

Mohamed Khider University of Biskra Faculty of exact sciences department of Matter sciences

MASTER MEMORY

MATTER SCIENCES CHEMISTRY MATERIALS CHEMISTRY

Réf.:

Presented by: **TERKI Aymen**

THE:

Experimental and Theoretical Study of complex perovskites

Jury:

| Dr. | OMARI Mahmoud | Professor Emeritus | University of BISKRA | President |
|-----|------------------|--------------------|----------------------|------------|
| Dr. | NEBBACHE Nadia | Professor | University of BISKRA | Examiner |
| Dr. | MAKHLOUFI Rachid | Senior Lecturer | University of BISKRA | Supervisor |

AcademicYear: 2024/2025

Acknowledgment

First and foremost, I express my deepest gratitude to Allah for granting me the strength, patience, and determination to complete this research work. I also extend sincere thanks to my family for providing conducive environment for study.

I would like to express my heartfelt appreciation to my supervisor, Dr. Makhloufi
Rachid, for his kindness, valuable guidance, and continuous support, as well as for
his tremendous efforts in sending samples for characterization and providing
everything necessary to complete this work.

I am also grateful to the members of the jury: Dr. Omari Mahmoud, Professor emeritus at Biskra university, for the honor of presiding over my thesis defense, Dr. Nebbache Nadiaa, Professor at Biskra university, for kindly accepting to evaluate and discuss my work.

A special thanks goes to Charif Rania, the doctoral student, for her kindness, support, and helping me quickly adapt, as well as for her efforts in sample characterization and her continuous guidance. I also thank Salma Omnia Racha, the doctoral student, for her kind assistance and for transporting the samples abroad for XRPD characterization.

I would like also to thank:

Mr. Gasmi Ibrahim for XRPD characterization.

Dr. Bala Saliha for UV-Visible and FTIR characterization.

Dr. Omari Lyes and Dr. Makhloufi Soufiane for allowing us to use Furnace(>1300 °C).

We thank all members of the pedagogical laboratory of Chemistry, Department of Matter science. And also all members of the laboratory LCA Applied Chemistry laboratory, for their cooperation and providing the appropriate environment for study and research.

Dedication

I dedicate this work:

To my dear parents, their tireless efforts, boundless patience, and unwavering support over the years have brought me to where I am today. This is a tribute to my deep love and profound respect for their immense sacrifices.

To my beloved sister HANIA and my dear brother MEHDI, for their constant love and support. May this serve as an expression of my heartfelt appreciation.

To my superviser, Rachid Makhloufi, who treated me like a son throughout this journey.

To my entire family, all my friends, and everyone dear to me.

To all my teachers throughout my university career.

To all my classmates in the Master's Degree in Materials Chemistry, Class of 2025, and to the rest of my fellow graduates, both within and beyond the Department of Matter Sciences.

TERKI AYMEN

Content:

| LIST OF FIGURES |
|---|
| LIST OF TABLES |
| LIST OF ABBREVIATIONS |
| GENERAL INTRODUCTION |
| Bibliographic References |
| Chapter I: General background of complex perovskites |
| I.1. Simple perovskites |
| I.2. Complex perovskites |
| I.2.1. Double perovskites |
| I.2.2. Layered perovskites |
| I.2.3. Triple perovskites9 |
| I.2.3.1. Triple perovskite formulas9 |
| I.2.3.2. Properties of triple Perovskites |
| I.2.3.3. Applications of triple perovskites |
| I.3. Triple perovskites with general formula A ₂ A'BB'B"O ₉ 14 |
| Dibliographia Deferences |

| II.1. Synthesis and characterization | 20 |
|--|----|
| II.1.1. Synthesis by Solid-State Reaction. | 20 |
| II.1.2. X-ray powder diffraction | 24 |
| II.1.3. Fourier Transform Infrared Spectroscopy (FTIR) | 26 |
| II.1.4. UV-Visible Spectroscopy | 28 |
| II.2. Computational code and methods | 32 |
| II.2.1. Density Functional Theory | 32 |
| II.2.1.1. Kohn-Hohenberg first theorem | 32 |
| II.2.1.2. Kohn-Hohenberg second theorem | 33 |
| II.2.1.3. Exchange-Correlation Functional | 34 |
| II.2.2. Pseudopotential | 36 |
| II.2.2.1. Pseudopotential principle | 36 |
| II.2.2.1. Pseudopotential types | 36 |
| II.2.3. Calculation code | 38 |
| II.2.4. Properties | 39 |
| II.2.4.1. Structural properties | 39 |
| II.2.4.2. Electronic properties | 40 |
| II.2.4.3. Optical properties | 41 |
| II.2.4.4. Mechanical properties | 44 |
| II.2.4.5. Phonon | 47 |
| Bibliographic References | 48 |

Chapter III: Results and discussions

| III.1. Synthesis and characterization | 51 |
|---|----|
| III.1.1. Synthesis steps | 51 |
| III.1.2. X-ray powder diffraction | 54 |
| III.1.3. Fourier Transform Infrared Spectroscopy (FTIR) | 58 |
| III.1.4. UV-Visible Spectroscopy | 59 |
| III.2. Computational results | 61 |
| III.2.1. Structural properties | 61 |
| III.2.2. Electronic properties | 63 |
| III.2.3. Optical Properties | 64 |
| III.2.4. Mechanical properties | 72 |
| III.2.5. Phonon | 77 |
| Bibliographic References | 78 |
| GENERAL CONCLUSION | 79 |

LIST OF FIGURES

| Figure I.1. Some applications of triple perovskites | 13 |
|---|-------------|
| Figure II.1. Programmable Furnaces used for heat treatment | 22 |
| Figure II.2. Schematic of the calcination thermal cycle | 22 |
| Figure II.3. Principle of Bragg's law | 24 |
| Figure II.4. MiniFlex Benchtop XRPD Instrument | 25 |
| Figure II.5. PerkinElmer spectrum two instrument | 27 |
| Figure II.6. Evolution 220 UV-Visible spectrophotometer instrument | 28 |
| Figure II.7. Comparison between direct and indirect band gap | 30 |
| Figure III.1. Magnetic Stirring Setup | 51 |
| Figure III.2. Oven used for drying the powder mixture | 52 |
| Figure III.3. Powder after grinding in a glass mortar | 52 |
| Figure III.4. Pellets of Compound N°1 and N°2 | 53 |
| Figure III.5. XRPD patterns of Compound N°1 at different synthesis temperatures | 54 |
| Figure III.6. Comparison of experimental XRPD pattern with calculated patterns | 55 |
| Figure III.7. XRPD patterns of Compound N°2 at 1200 °C and 1290 °C | 56 |
| Figure III.8. Comparison of experimental XRPD pattern with calculated patterns | 57 |
| Figure III.9. FTIR spectra of Compound N°1 and Compound N°2 | 58 |
| Figure III.10. UV-Visible Absorption Spectra of Compound N°1 and Compound N°2 | 2 59 |
| Figure III.11. Tauc plots of $(\alpha h v)^2$ and $(\alpha h v)^{1/2}$ for direct and indirect transitions | 60 |

| Figure III.12. Band structure of Compound N°1 and Compound N°263 |
|---|
| Figure III.13. TDOS of the triple perovskites Compound N°1 and Compound N°264 |
| Figure III.14. The dielectric function (real and imaginary part) of Compound N°1 and Compound N°2 |
| Figure III.15. Refractive index (n) and extinction coefficient (k) of Compound N°1 and Compound N°2 |
| Figure III.16. Reflectivity behavior of Compound N°1 and Compound N°267 |
| Figure III.17. Absorption coefficient behavior of Compound N°1 and Compound N°268 |
| Figure III.18. Energy loss function for Compound N°1 and Compound N°269 |
| Figure III.19. Optical conductivity (real and imaginary part) profile of Compound N°1 and Compound N°2 |
| Figure III.20. Poisson's and Pugh's Ratios for Compound N°1 and Compound N°275 |
| Figure III.21. Phonon dispersion of Compound N°2 |

LIST OF TABLES

| Table III.1. Supercell lattice parameters of Compound $N^{\circ}1$ and Compound $N^{\circ}2$ before |
|---|
| and after optimization63 |
| Table III.2. The computed elastic constants of Compound N°1 and Compound N°2 76 |
| Table III.3. Calculated Eigenvalues (λ) of Compound N°1 and Compound N°2 77 |
| Table III.4. Elastic and Mechanical Parameters of Compound N°1 and Compound N°2 78 |

LIST OF ABREVIATIONS

XRPD X-Ray Powder Diffraction

XRD X-Ray Diffraction

FTIR Fourier Transform Infra-Red

UV Ultra-Violet

EUV Extreme Ultra-Violet

CASTEP Cambridge Serial Total Energy Package

DFT Density Functional Theory

 E_{XC} Exchange-Correlation Energy

LDA Local Density Approximation

GGA Generalized Gradient Approximation

PBE Perdew-Burke-Ernzerhof

PAW Projector Augmented-Wave

FLAPW Full-potential Linearized Augmented Plane

Wave

USPPs Ultra-Soft Pseudo-Potentials

NCPPs Norm-Conserving Pseudo-Potentials

OTFG On-The-Fly Generation

TDOS Total Density Of State

PDOS Partial Density Of State

VB Valence Band

CB Conduction Band

GENERAL INTRODUCTION

GENERAL INTRODUCTION

Perovskite oxides represent a large percentage of systems currently studied and continue to interest scientists. Perovskite oxides have characterized by the formula ABO₃, where A is a relatively large cation of alkalin, alkaline earth or rare earth metals, occupies a twelve coordinate site, B is a smaller cation of transition metals, which occupies an octahedral coordinate site.

The properties of perovskites are strongly dependent on the cations occupying the A and B sites, their electronic configurations and interactions[1, 2]. Consequently, the fundamental perovskite structure (ABO₃) can be significantly diversified by incorporating various cations into the A and B sites of the primitive perovskite unit cell. This leads to the formation of complex perovskites, including double and triple perovskites, which exhibit a wide range of chemical formulas, such as A₂BB'O₆, AA'B₂O₆, A₃B₂B'O₉, A₃BB'B"O₉, and A₂A'B₂B'O₉.

Complex perovskites display a richer array of properties compared to the fundamental structure of simple perovskites. Double and triple perovskites, in particular, can integrate diverse functional characteristics within a single compound. Furthermore, complex perovskites exhibit tunable properties in response to variations in external conditions such as temperature and pressure. Notably, they have also emerged as safer alternatives to certain simple perovskites containing toxic elements[3]. These attributes have established complex perovskites as crucial materials in numerous industrial applications.

Among these, triple perovskites represent an exciting frontier, offering enhanced compositional flexibility through the ordered arrangement of three distinct B-site cations. While double perovskites have been extensively studied for their multifunctional behavior [4-6], triple perovskites remain relatively underexplored[7].

Despite their potential, previous studies on triple perovskites have primarily focused on synthesis and basic experimental characterization, the computational cost of these complex systems is a real obstacle. Unfortunately, there is hardly a single article that combines experimental and computational study, leaving gaps in understanding their properties and applications.

General Introduction

Addressing these gaps requires a synergistic approach, combining experimental synthesis and characterization with first-principles calculations to establish a comprehensive understanding of these materials.

This thesis aims to bridge these knowledge gaps through the synthesis and structural characterization of phase-pure two triple perovskites via solid-state reaction, validated by X-ray diffraction (XRD), UV-Visible spectroscopy and Fourier-transform infrared spectroscopy (FTIR). This is accompanied by the computational exploration of their structural, electronic, optical, and mechanical properties using density functional theory (DFT) as implemented in the CASTEP code with the GGA-PBE functional. By correlating experimental and computational results, this work seeks to elucidate how cation ordering and B-site chemistry govern the physical properties of these triple perovskites.

The significance of this study lies in its dual experimental-theoretical approach, which provides first-reported insights into two compounds optical absorption, elastic properties, and phonon dynamics. Additionally, the findings may guide future design strategies for tailored perovskite materials, particularly in applications requiring precise control over electronic or thermal transport. The rarity of computational studies on such systems further underscores the novelty of this work, offering a foundation for future investigations into complex perovskite oxides.

The thesis is structured into three chapters. Chapter 1 introduces the broader landscape of perovskite materials, progressing from simple to double and triple perovskites, and concludes with a focus on the structural parameters of our compounds. Chapter 2 details the experimental methods (solid-state synthesis, XRD, FTIR, UV-Vis spectroscopy) and computational framework (DFT methodology, property prediction techniques). Finally, Chapter 3 presents the results and discussion, comparing experimental and theoretical findings.

By integrating synthesis, characterization, and modeling, this work not only advances fundamental knowledge of triple perovskites but also paves the way for their targeted application in next-generation functional materials.

Bibliographic references:

- [1] S. Guo, H. Wu, F. Puleo, L.F. Liotta, B-Site Metal (Pd, Pt, Ag, Cu, Zn, Ni) Promoted La1– x Sr x Co1– y Fe y O3– δ Perovskite Oxides as Cathodes for IT-SOFCs, Article, Catalysts, 5 (2015).
- [2] X. Li, H. Zhao, J. Liang, Y. Luo, G. Chen, X. Shi, S. Lu, S. Gao, J. Hu, Q. Liu, A-site perovskite oxides: an emerging functional material for electrocatalysis and photocatalysis, Article, Journal of materials chemistry A, 9 (2021).
- [3] P.-K. Kung, M.-H. Li, P.-Y. Lin, J.-Y. Jhang, M. Pantaler, D.C. Lupascu, G. Grancini, P. Chen, Lead-free double perovskites for perovskite solar cells, Article, Solar RRL, 4 (2020).
- [4] S.A. Dar, G. Murtaza, T. Zelai, G. Nazir, H. Alkhaldi, H. Albalawi, N.A. Kattan, M. Irfan, Q. Mahmood, Z. Mahmoud, Study of structural, electronic, magnetic, and optical properties of A2FeMnO6 (A= Ba, La) double perovskites, experimental and DFT analysis, Article, Colloids and Surfaces A: Physicochemical and Engineering Aspects, 664 (2023).
- [5] M. Elhamel, Z. Hebboul, M.E. Naidjate, A. Draoui, A. Benghia, M. abdelilah Fadla, M.B. Kanoun, S. Goumri-Said, Experimental synthesis of double perovskite functional nano-ceramic Eu2NiMnO6: combining optical characterization and DFT calculations, Article, Journal of Solid State Chemistry, 323 (2023).
- [6] M. Irfan, G. Murtaza, N. Muhammad, S. Tahir, H.H. Raza, B. Sabir, M. Iftikhar, S. Sharif, Experimental and theoretical studies of structural, electronic and magnetic properties of RE2NiCrO6 (RE= ce, Pr and Nd) double perovskites, Article, Physica E: Low-dimensional Systems and Nanostructures, 148 (2023).
- [7] W. González, R. Cardona, D.L. Téllez, J. Roa-Rojas, Crystallographic and electronic structure of the Sr3Sb2CoO9 triple perovskite, Conference, Journal of Physics Conference Series (2014).

CHAPTER I

General Background of Complex Perovskites

The study of perovskites has long captivated materials scientists. The perovskite structure is renowned for its versatility, exhibiting a wide array of physical and chemical properties that enable applications across numerous fields.

In the 19th century, the fundamental perovskite structure, now termed "simple perovskite", was identified. Its distinctive geometry and properties spurred extensive research, leading to the discovery and synthesis of more intricate variations, known as "complex perovskites".

While this work centers on "triple perovskites", a subset of complex perovskites, a thorough understanding of the foundational simple perovskite structure remains crucial.

I.1. Simple perovskites:

The perovskite-type structure holds a significant position within the ternary family of crystalline structures. The term "Perovskite" originally referred to a rare mineral, calcium titanate (CaTiO₃), which was discovered in 1839 by the German chemist Gustav Rose. It was named "Perovskite" in honor of the Russian mineralogist Lev Alexeievitch Perovski[1]. However, today, the term "perovskite" refers to a broader group of compounds that share the same atomic arrangement, with the general formula ABX₃.

In the perovskite structure, we can distinguish three types of sites:

- A-sites: These sites have either eight or twelve coordinations (AX₈ or AX₁₂). They are typically occupied by alkali metals, alkaline earth metals, or rare earth metals. These sites can accommodate large-sized cations with one, two, or three valence oxidation states[1].
 - This type of site is crucial for determining the stability of the perovskite lattice. They can also influence catalytic activity and electronic properties in some cases (A-site cations with large π -conjugated structures).
- ➤ B-sites: These sites have six coordinations (AX₆). They are primarily occupied by transition metals and can host small-sized cations with oxidation states ranging from one to six[1].
 - B-site atoms play an important role in determining the properties of perovskites, such as electronic, magnetic, and optoelectronic properties. These properties depend on the specific atoms that occupy this site.

➤ X-sites: These sites are occupied by anions such as O²-, F-, Cl- or I-. Each X anion is surrounded by two B-site cations and four A-site cations[2].

The term "perovskite oxide" specifically refers to perovskites where X-sites are occupied by oxygen ions. These compounds are typically represented by the chemical formula ABO₃.

The ideal perovskite structure is described by a cubic unit cell belonging to the space group "Pm3m". In this structure, the A atoms occupy the vertices of the cube, the B atoms are located at the center, and the oxygen atoms are positioned at the face centers. The ideal cubic perovskite structure (Pm3m) exhibits the highest symmetry. However, lower symmetry structures can arise due to three main effects:

Cation ordering in A or B sites (e.g., Ba₂MnWO₆, space group Fm3m)[2].

Octahedral tilting (e.g., La₃Ni₂SbO₉, space group P2₁/n)[2].

Jahn-Teller distortions (e.g., La₂CuSnO₆, space group P4/mmm)[2].

Due to the vast number of possible combinations of A and B cations and X anions, perovskite materials exhibit a wide range of physical and chemical properties. These include relaxor ferroelectricity, relaxor ferromagnetism, multiferroicity, catalytic activity, superconductivity, antiferromagnetism, ferroelectricity, and more. Consequently, perovskites have found extensive use in various technological applications, such as relaxor materials, piezoelectric materials, magnetic memories, dielectrics, and electrolyte materials.

Of course, perovskite structures must adhere to the "charge neutrality rule", considering that many elements in the periodic table exhibit multiple oxidation states (either integer or fractional)[2].

I.2. Complex perovskites:

The ideal stoichiometry of a perovskite (ABX₃) can be modified by substituting one, two, or three different types of cations at the A or B positions. This structural flexibility allows perovskites to adopt more complex perovskite types[2]. Such as double, triple and layered perovskites, with so many formulas.

I.2.1. Double perovskites:

In the early days of perovskite research, research focused on replacing simple perovskite components. For example, complex perovskites are formed by doping (partial replacement) of one or both A and B sites, in varying proportions.

Double perovskites describe the perovskites with A or B site (or both) occupied by two different types of cations, this leads to various chemical formulas, including $A_2BB'X_6$, $AA'B_2X_6$, and $AA'BB'X_6[3]$.

The term "double perovskite" describes the increased complexity in the cation arrangement within the perovskite structure. It refers to the fact that each unit cell of a double perovskite is formed by combining two basic simple perovskite unit cells.

Research into double perovskites, with the general formula A₂BB'X₆, began in earnest in the early 1950s. This was followed by the emergence of more complex and diverse formulas, such as AA'B₂X₆, and AA'BB'X₆. Double perovskites came with interesting properties, and it gained attention for their magnetic and electronic properties.

Double perovskites have improved many properties compared to simple perovskites which has produced new application areas, and have helped replace some toxic lead-based compounds (Some double perovskites do not match the efficiency of lead-based perovskites in solar cells yet).

Considering its properties, double perovskite can be used in several applications, such as: solar cells, light-emitting diodes (LEDs), photodetectors, spintronics...etc.

I.2.2. Layered perovskites:

While double and triple perovskites are described as 3D perovskites, there are also layered perovskites, which are more accurately classified as quasi-2D perovskites.

The term "layered perovskites" specifically refers to structures where the 3D connectivity of the BX₆ octahedra is disrupted, resulting in a quasi-2D or sheet-like structure. Conceptually, these structures can be understood as being derived from a 3D perovskite by slicing and introducing structural features that reduce the dimensionality[4].

Layered perovskites follow the general formula $A_{n+1}B_nX_{3n+1}$, where n=1, 2, 3, etc. Classical examples include K_2NiF_4 , La_2CuO_4 , and $Sr_3Ti_2O_7$, which belong to the Ruddlesden-Popper (RP) series of compounds, etc[4].

I.2.3. Triple perovskites:

Triple perovskites have attracted significant research interest due to their novel and promising physical properties, research into these materials has increased significantly in the more recent decades, as advances in synthesis and characterization techniques have made them more accessible.

Triple perovskites came after the double perovskites, they are an extension of the double perovskite concept, involving even more complex arrangements of cations.

The term "triple perovskite" arises because, while a standard unit cell can be used for initial structural analysis, a more comprehensive description of these perovskites necessitates the use of a "supercell". This supercell is constructed by replicating the fundamental perovskite unit cell three times in a chosen crystallographic direction.

I.2.3.1. Triple perovskite formulas:

For triple perovskites, we can define so many formulas for triple perovskites structures, such as: A₃B₂B'O₉, A₂A'B₂B'O₉, A₃BB'B"O₉ and A₂A'BB'B"O₉.

A₃B₂B'O₉: this formula has two different B-site cations, with different propotions (2/3 for B cation, 1/3 for B' cation), this formula is very common, we can have so many examples: Sr₃Fe₂TeO₉[5], Ba₃Fe₂TeO₉[5], Sr₃Sb₂CoO₉[6].

A₂A'B₂B'O₉: this formula has two different B-site and A-site cations, with different propotions also (2/3 for A and B cations, 1/3 for A' and B' cations), this formula is also very common, it appears from substituting one A and B cations by A' and B' cations respectively, we give those examples: La₂SrFe₂CoO₉ [7], Y₂SrFe₂ZrO₉ [8], Sr₂CaFe₂WO₉[9] and BaSr₂MgTa₂O₉[10].

A₃BB'B"O₉: this formula has three different B-site cations, all with the same propotions (1/3 for all of B, B', B'' cations), it's less common than previous formulas, but it can results various properties, such as: Ba₃NiTaNbO₉ and Ba₃NiTaSbO₉[11].

A₂A'BB'B"O₉: this formula has two different A-site cations, with different propotions (2/3 for A cation, and 1/3 for A' cation). And three different B-site cations, with the same propotions (1/3 for all B, B' and B" cations), this formula is not commonly studied, these are some examples of this formula: SrLa₂FeCuSbO₉ [12], CaLa₂FeCoSbO₉ [5] and BaLa₂FeNiSbO₉[5].

Triple perovskites can also be written using a unit cell instead of a supercell. Although this type of writing is not very common, for example, $Ca(Zn_{1/3}Ta_{2/3})O_3$ can be written as the same as $Ca_3(ZnTa_2)O_9$.

I.2.3.2. Properties of triple perovskites:

Triple perovskites crystallize in a range of structures, including cubic, tetragonal, orthorhombic, monoclinic, (the most common), and rarely, triclinic. This polymorphism, in conjunction with the compositional flexibility afforded by diverse cation substitutions at the A and B sites, leads to a wide array of achievable properties.

I.2.3.2.1. Electronic properties:

The electronic properties basically depend on the triple perovskite compositions. Acording to the gap energy value, a triple perovskite can be:

- ► Metal: corresponds to $E_g \approx 0$ eV , such as $Sr_3Sb_2CoO_9[13]$.
- > Semiconductor: corresponds to $0 \text{ eV} \le E_g \le 3 \text{ eV}$, such as: Ba₃CaMo₂O₉, Ba₃CaRh₂O₉[14] and Ba₂K₂Te₂O₉[15].
- ► Insulator: corresponds to $E_g > 3 \text{ eV}$, such as: Ba₃CaNb₂O₉[14].

I.2.3.2.2. Optical properties:

Triple perovskite compounds exhibit a broad range of optical properties due to their compositional flexibility and structural complexity. These properties arise from their ability to interact with light across different regions of the electromagnetic spectrum. Below are some examples of notable optical properties observed in triple perovskites:

- ➤ Light Absorption: Certain types of triple perovskites can strongly absorb light in the ultraviolet such as Ba₃CaMo₂O₉ and Ba₃CaNb₂O₉ [14], visible, or even near-infrared regions.
- ➤ Optical Band Gap Behavior: These materials often exhibit tunable band gaps depending on their composition, enabling control over the specific wavelengths of light they absorb or transmit. Such as Ba₃CaNb₂O₉[14].
- ➤ Light Scattering and Reflectance: Depending on their microstructure and surface morphology, triple perovskites may scatter or reflect light in characteristic ways.

I.2.3.2.3. Magnetic properties:

Triple perovskites exhibit remarkable magnetic properties due to the diversity of B-site cations, where three different cations can coexist within the same crystal structure. This structural flexibility enables strong electronic interactions, leading to a wide range of magnetic behaviors, including:

- Ferromagnetism; such as La₂SrFe₂TiO₉ and La₂SrFe₂CoO₉[16].
- Ferrimagnetism; such as SrLa₂FeCoSbO₉[17].
- Paramagnetic; such as Ba₃ZrRu₂O₉[18].
- Antiferromagnetism; such as Ba₃TiRu₂O₉[18].

I.2.3.2.4. Dielectric properties:

Triple perovskite compounds also demonstrate diverse dielectric properties, stemming from their complex crystal structures and the interactions among their multiple cationic sites. Below are some key dielectric characteristics observed in triple perovskites:

- ➤ High Dielectric Constant: Many triple perovskites exhibit relatively high dielectric constants, such as Ba₃CaRh₂O₉ [14].
- ➤ Frequency-Dependent Behavior: The dielectric response of these materials often varies with the frequency of the applied electric field.

> Temperature-Dependent Permittivity: Their dielectric permittivity may change significantly with temperature.

I.2.3.2.4. Mechanical properties:

Triple perovskite compounds exhibit a variety of mechanical properties that are influenced by their complex crystal structures and multi-element compositions. The main mechanical characteristics observed in triple perovskites include:

- Mechanical Stability: Based on elastic constants, the mechanical stability of these materials can be assessed using established criteria.
- ➤ Brittle or Ductile Nature: Depending on the bonding characteristics and atomic arrangement, triple perovskites may exhibit either brittle or ductile behavior.
- Anisotropy: Due to their complex cation ordering, triple perovskites may show anisotropic mechanical responses, meaning their stiffness or compressibility varies with direction.
- Hardness: The intrinsic hardness of triple perovskites, which relates to their resistance to localized deformation or scratching, can also be compositiondependent.

I.2.3.3. Applications of triple perovskites:

The applications of triple perovskites are diverse and largely depend on their intrinsic properties.

Given the electronic properties of triple perovskites, they can be used in many fields. The metallic property is widely used in the manufacture of batteries and fuel cells, on the other hand, transistors are based on the semi-conductive nature of the triple perovskite, semi-conductors can also be used in the manufacture of batteries.

Some optical properties are very important, triple perovskites which have strong light absorption and high exciton binding energy are exploited for solar cells manufacturing, while triple perovskites which have other type of optical properties such as wide spectral absorption, fast response time, high carrier mobility are used in Photodetectors.

Capacitors are primarily manufactured based on the dielectric properties of triple perovskites, which must possess high dielectric constant and low loss.

The magnetic properties of triple perovskites have various uses. Some industries may rely on the ferromagnetism property of perovskites, such as magnetic storage, while other industries rely on the antiferromagnetism property of perovskites, such as sensors... etc.

In addition, the mechanical properties of triple perovskites (such as high hardness, elastic modulus, and structural stability) make them suitable for applications in harsh environments, including aerospace structural components, protective or wear-resistant coatings, microelectromechanical systems (MEMS), and mechanical actuators, where durability and resistance to stress are essential.

While the applications mentioned above are driven by specific functional properties, the versatility of triple perovskites goes beyond these examples. Although certain simple perovskites may possess comparable optical properties to complex ones, they often lack the favorable magnetic, electronic or mechanical characteristics necessary for broader use. One of the key advantages of complex perovskites (especially triple perovskites) is their ability to combine multiple desirable properties in a single material. This multifunctionality makes them highly attractive for the design of advanced devices that require a synergistic combination of optical, electronic, magnetic, and mechanical performance.



Figure I.1. Some applications of triple perovskites.

I.3. Triple perovskites with general formula A₂A'BB'B"O₉:

Triple perovskites with the general formula A₂A'BB'B"O₉ have attracted significant interest due to their tunable structural, electronic, magnetic, and optical properties. This versatility arises from the large number of possible combinations of cations that can occupy both the A and B sites. However, the synthesis of such compounds is often challenging because the incorporation of multiple elements can lead to cation ordering issues and structural complexity.

The A₂A'BB'B"O₉ formula has two different A-site cations, with different propotions (2/3 for A cation, and 1/3 for A' cation). And three different B-site cations, with the same propotions (1/3 for all B, B' and B'' cations).

Previous studies on compounds such as $SrLa_2FeNiSbO_9$ [19], $SrLa_2FeCoSbO_9$ [5], and $SrLa_2FeCuSbO_9$ [12] have shown that they typically crystallize in a monoclinic structure with space group $P2_1/n$. The lattice parameters are unequal ($a \neq b \neq c$) with angles $\alpha = \gamma = 90^{\circ} \neq \beta$. Interestingly, the monoclinic angle β is very close to 90° , for example:

```
\beta = 90.094° for SrLa<sub>2</sub>FeCuSbO<sub>9</sub> [12].
```

Due to this near-orthogonal symmetry, the X-ray diffraction (XRD) patterns of monoclinic and orthorhombic systems often appear similar. As a result, neutron diffraction is typically required to accurately determine the crystal structure, which had been used to identify the crystallin system of the triple perovskites mentioned before [5, 19].

 $[\]beta$ = 89.98° for SrLa₂FeNiSbO₉ [19].

 $[\]beta$ = 90.050° for SrLa₂FeCoSbO₉ [5].

| Chapter 1: General background of complex perovskites | | | | | |
|--|--|--|--|--|--|
| | | | | | |
| | | | | | |
| | | | | | |
| | | | | | |
| | | | | | |
| | | | | | |
| | | | | | |
| | | | | | |
| | | | | | |
| | | | | | |
| | | | | | |
| | | | | | |
| | | | | | |
| | | | | | |
| | | | | | |
| | | | | | |
| | | | | | |
| | | | | | |
| | | | | | |
| | | | | | |
| | | | | | |
| | | | | | |
| | | | | | |
| | | | | | |
| | | | | | |
| | | | | | |
| | | | | | |
| | | | | | |
| | | | | | |
| | | | | | |
| | | | | | |
| | | | | | |
| | | | | | |
| | | | | | |
| | | | | | |
| | | | | | |
| | | | | | |
| | | | | | |
| | | | | | |

| Chapter I: General background of complex perovskites | | | | |
|--|--|--|--|--|
| | | | | |
| | | | | |
| | | | | |
| | | | | |
| | | | | |
| | | | | |
| | | | | |
| | | | | |
| | | | | |
| | | | | |
| | | | | |
| | | | | |
| | | | | |
| | | | | |
| | | | | |
| | | | | |
| | | | | |
| | | | | |
| | | | | |
| | | | | |
| | | | | |
| | | | | |
| | | | | |
| | | | | |
| | | | | |
| | | | | |
| | | | | |
| | | | | |

Bibliographic references:

- [1] C. Moure, O. Peña, Recent advances in perovskites: Processing and properties, Article, Progress in Solid State Chemistry, 43 (2015).
- [2] R. Paria Sena, Structure characterization of triple perovskites and related systems by transmission electron microscopy, Thesis, University of Antwerp (2017).
- [3] W.-J. Yin, B. Weng, J. Ge, Q. Sun, Z. Li, Y. Yan, Oxide perovskites, double perovskites and derivatives for electrocatalysis, photocatalysis, and photovoltaics, Article, Energy & Environmental Science, 12 (2019).
- [4] H.A. Evans, L. Mao, R. Seshadri, A.K. Cheetham, Layered double perovskites, Article, Annual Review of Materials Research, 51 (2021).
- [5] Y. Tang, Synthesis and characterisation of iron-containing perovskites, Thesis, University of Oxford (2018).
- [6] S.A. Fatima, R. Shaheen, K. Shahzad, Study of electrical and dielectric properties of Sr3CoSb2O9 perovskite by impedance spectroscopy, Article, Applied Physics A, 127 (2021).
- [7] F. Casallas, E. Vera, D. Landinez, C. Parra, J. Roa, Structural properties, electric response and magnetic behaviour of La2SrFe2CoO9 triple complex perovskite, Conference, Journal of Physics Conference Series (2016).
- [8] F. Nekkach, H. Lemziouka, A. Boutahar, M. El Yazidi, Study of the optical properties of sol-gel prepared perovskite Y2SrFe2ZrO9: Towards innovative applications in optoelectronics and solar energy, Article, Optical Materials, 159 (2025).
- [9] Y. Arba, Z. Yamkane, J. Louafi, A. Elouafi, A. El Hachmi, S. El Ouahbi, B. Manoun, R. Moubah, L. Omari, H. Lassri, Optical properties investigation of Sr2CaFe2WO9 triple perovskite for optoelectronic applications, Article, Optik, 288 (2023).
- [10] M.R. Imer, L. Suescun, F.A. Rabuffetti, Structure of triple perovskite BaSr2MgTa2O9 revisited, Article, Journal of Solid State Chemistry, 306 (2022).
- [11] A. Barua, S. Dey, S. Sabyasachi, S. Kumar, Structural and dielectric characterization of triple perovskites Ba3NiTaNbO9 and Ba3NiTaSbO9, Article, Journal of Alloys and Compounds, 854 (2021).
- [12] N. Boudar, B. Mehdaoui, A. Aatiq, Structural and Magnetic Properties of the New SrLa 2 FeCuSbO 9 Perovskite Phase, Article, Journal of Superconductivity and Novel Magnetism, 33 (2020).
- [13] W. González, R. Cardona, D.L. Téllez, J. Roa-Rojas, Crystallographic and electronic structure of the Sr3Sb2CoO9 triple perovskite, Conference, Journal of Physics Conference Series (2014).
- [14] B. Hassan, M. Irfan, M. Aslam, E. Buntov, The electronic structure, electronic charge density, optical and thermoelectric properties of Mo and Rh based triple perovskite semiconductors Ba3CaNb2O9 for low-cost energy technologies, Article, Optical and Quantum Electronics, 56 (2024).

- [15] A. Kushwaha, Ş. Uğur, M. Güler, E. Güler, G. Uğur, First principles investigations of structural, elastic, mechanical, electronic and optical properties of triple perovskite Ba2K2Te2O9, Article, Physica B: Condensed Matter, 596 (2020).
- [16] F.M. Casallas, E. Vera-Lópeza, D.L. Téllez, D.S. Mesa, J. Roa-Rojas, Magnetic feature, compositional and structural analysis of the La2SrFe2CoO9 complex perovskite, Conference, Journal of Physics Conference Series (2014).
- [17] Y. Tang, E.C. Hunter, P.D. Battle, M. Hendrickx, J. Hadermann, J. Cadogan, Ferrimagnetism as a consequence of unusual cation ordering in the perovskite SrLa2FeCoSbO9, Article, Inorganic chemistry, 57 (2018).
- [18] R. Zada, Z. Ali, S. Mehmood, DFT Study of the Structural and Magnetic Properties of Triple Perovskites Ba3TiRu2O9 and Ba3ZrRu2O9, Article, Journal of Inorganic and Organometallic Polymers and Materials, 34 (2024).
- [19] M. Hendrickx, Y. Tang, E.C. Hunter, P.D. Battle, J. Cadogan, J. Hadermann, CaLa2FeCoSbO9 and ALa2FeNiSbO9 (A= Ca, Sr, Ba): cation-ordered, inhomogeneous, ferrimagnetic perovskites, Article, Journal of Solid State Chemistry, 285 (2020).

CHAPTER II

Experimental and Computational Methods

This chapter outlines the methodologies employed in the present study, which integrates both experimental procedures and first-principles calculations to investigate the structural, electronic, and optical properties of the studied perovskite materials.

The experimental section focuses on the synthesis of the compounds using conventional solid-state reaction methods, followed by structural and compositional characterization through X-ray powder diffraction (XRPD) and Fourier-transform infrared spectroscopy (FTIR), as well as optical characterization via ultraviolet (UV) spectroscopy. These techniques provide insights into phase purity, crystallinity, functional groups, and electronic transitions.

On the theoretical side, density functional theory (DFT)-based calculations were performed using the CASTEP code to gain a deeper understanding of the electronic structure and optical behavior of the compounds. The calculations were carried out using the generalized gradient approximation (GGA) within the Perdew–Burke–Ernzerhof (PBE) framework, with appropriate parameters for energy cut-off and Brillouin zone sampling.

Together, the experimental and theoretical methods described in this chapter provide the basis for the results and discussions that follow in the next chapter (Chapter III).

II.1. Synthesis and characterization:

II.1.1. Synthesis by Solid-State Reaction:

Solid-state synthesis is one of the most widely used methods in solid-state chemistry. In such reactions, nitrates, carbonates, oxides, and other compounds are mixed in stoichiometric ratios. This method relies on the thermal treatment of the mixture without reaching the melting point of the individual solids. After a sufficiently long heating period, a single-phase product is typically obtained [1].

The particle size distribution plays a crucial role in both the reaction rate and the homogeneity of the final product, as diffusion in the solid state is inherently slow. Therefore, it is essential that the starting materials are finely ground to reduce particle size. They must also be thoroughly mixed to maximize contact surface area and minimize diffusion distances between reactants. Frequently, the reaction mixture undergoes a preliminary calcination, is reground, and then reheated to renew the contact surfaces and accelerate the reaction.

One of the main advantages of this technique is its simplicity and ease of implementation, as it does not require prior chemical preparation of the precursors.

II.1.1.1. Raw materials:

The raw materials used include oxides, carbonates, nitrates, and similar compounds. An ideal powder consists of small, uniformly shaped grains (typically around 1 μ m in size) with a narrow particle size distribution. The purity of both the powder and any additives is carefully controlled.

A key challenge in working with powdered raw materials is the difficulty in evaluating the parameters that determine their reactivity. Consequently, the thermal history of the material significantly influences its behavior during the reaction.

II.1.1.2. Mixing and grinding:

This step aims to achieve a uniform distribution of the precursors. The powdered carbonate, oxide, and hydroxide precursors are weighed in stoichiometric proportions and mixed in a solvent inside a beaker. Homogenization is carried out using a magnetic stirrer.

The chosen solvent should have a low evaporation point to facilitate drying and must not react with any components of the mixture.

The resulting paste is dried to obtain a powder, which is then ground in a glass mortar for an adequate period to achieve the finest possible particle size. This fine powder promotes faster solid—solid phase formation through diffusion.

II.1.1.3. Calcination:

The purpose of calcination is to transform the powder mixture into a material with a well-defined composition and crystalline structure. For this purpose, the samples are placed in crucibles and subjected to a thermal cycle, during which solid-state diffusion leads to the formation of the desired phase. During this process, gases such as carbon dioxide, oxygen, and occasionally water vapor may be released.

Calcination is carried out using using two different programmable furnaces from Nabertherm, as shown in Figure II.1.



Figure II.1. Programmable Furnace used for heat treatment.

The thermal profile used for calcining the ground solid solution is illustrated in Figure II.2.

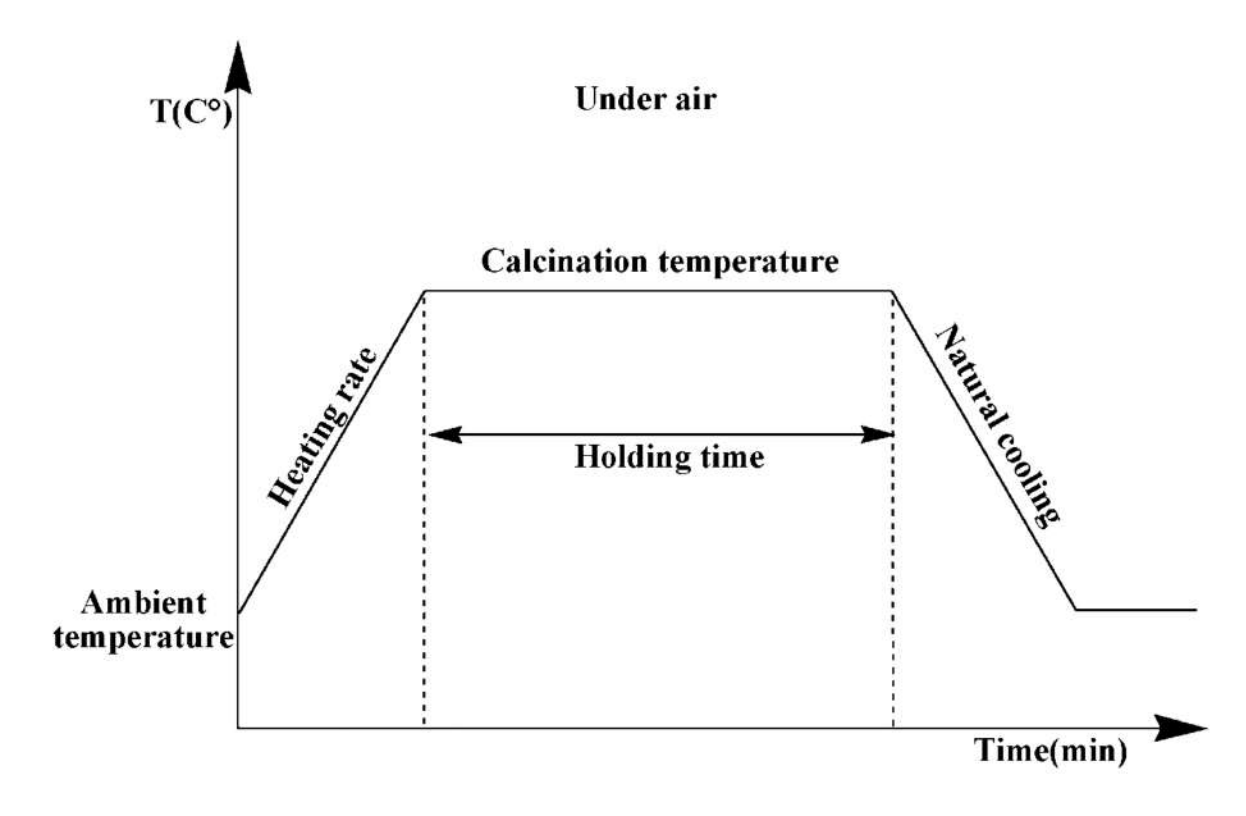


Figure II.2. Schematic of the calcination thermal cycle.

II.1.1.4. Regrinding:

After the initial heat treatment, the powder is subjected to regrinding. This step aims to break up agglomerates, homogenize the powder (particularly in cases where the initial reaction during chamotte grinding was incomplete) and reduce particle size to enhance reactivity. This regrinding is performed under the same conditions as the initial grinding step. Following regrinding, the powder undergoes a subsequent high-temperature treatment to facilitate the formation of the desired crystalline phases.

II.1.1.5. Sintering:

Sintering refers to a set of physical processes that transform a powder into a mechanically solid and cohesive structure. In certain cases, this transformation can occur without the application of external pressure, driven solely by high temperatures.

The primary objectives of this heat treatment are to complete the formation of the crystalline phase and to promote densification of the ceramic material. During sintering, the material is heated to a high temperature below its melting point, resulting in the strengthening of intergranular bonds, consolidation of the structure, and volumetric shrinkage.

The sintering process begins with the formation of "necks" between adjacent particles, which gives the material an initial mechanical strength while maintaining an open-pore structure. As the process progresses, grain growth and porosity elimination occur through complex mechanisms such as volume and surface diffusion. In the final stage, grain boundaries migrate, and grain size increases. Thus, sintering can be described as the thermal consolidation of a granular aggregate, with or without partial melting of its constituents [2].

Precise control of the sintering process is essential, as the outcome depends heavily on the thermal profile such as the heating rate and plateau duration, as well as the atmosphere in which sintering occurs. These parameters critically influence the final density, grain size, and compositional uniformity of the material.

As the final and crucial step in ceramic processing, sintering aims to produce a polycrystalline material with a well-defined geometry and microstructure at the lowest possible temperature.

II.1.2. X ray powder diffraction:

X-ray powder diffraction (XRPD) is a powerful and non-destructive technique widely used to investigate the structural properties of crystalline materials [3]. It is based on Bragg's law, which describes the diffraction of X-rays by atomic planes in a crystal when specific geometric conditions are met. The condition for constructive interference is defined by Bragg's equation [4]:

$$2d_{hkl}\sin\theta = n\lambda$$

Where " d_{hkl} " is the interplanar spacing, " θ " is the angle of incidence, " λ " is the X-ray wavelength, and "n" is the diffraction order.

In powder samples, which consist of numerous randomly oriented crystallites, there are always some crystallographic planes oriented such that they satisfy Bragg's condition. As a result, the diffracted X-rays produce a pattern of characteristic peaks corresponding to the material's crystal structure.

Figure II.3 illustrates this principle, showing how incident X-rays interact with different crystallographic planes to produce diffraction peaks when Bragg's condition is met.

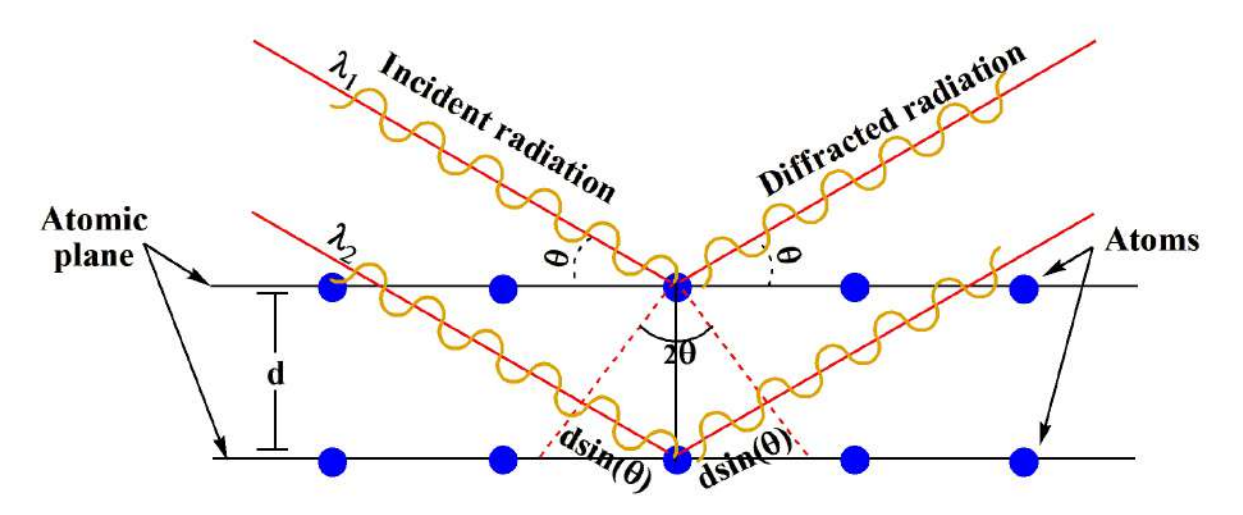


Figure II.3. Principle of Bragg's law.

When Bragg's condition is satisfied, constructive interference results in the appearance of diffraction peaks, enabling phase identification and structural analysis. This method provides essential information, including unit cell parameters, crystal symmetry, crystallite size, and internal strain [5].

The accuracy of the results strongly depends on proper sample preparation, as the position, intensity, and shape of the diffraction lines are highly sensitive to the quality of the sample.

Measurements were performed using a MiniFlex Benchtop X-ray Powder Diffraction (XRPD) Instrument (Rigaku), as shown in Figure II.4. This benchtop diffractometer utilizes a monochromatic X-ray beam directed at the sample. When the incident angle satisfies Bragg's condition, the diffracted rays produce intensity peaks that are detected and recorded as a diffractogram, showing the variation of intensity I_{hkl} with the diffraction angle $2\theta_{hkl}$ [4, 6]. This instrument enables precise phase identification and structural characterization of crystalline materials.



Figure II.4. MiniFlex Benchtop XRPD Instrument.

II.1.3. Fourier Transform Infrared Spectroscopy (FTIR):

Infrared spectroscopy is a widely employed characterization technique, essential for determining compositions by identifying specific atomic groups in a given phase. It also offers structural insights into molecules based on their vibrational properties.

Infrared (IR) radiation lies between the visible and microwave regions of the electromagnetic spectrum. This range is categorized into the near infrared (10000–4000 cm⁻¹), mid infrared (4000–400 cm⁻¹), and far infrared (400–50 cm⁻¹).

The most commonly used region is the one between 4000 and 400 cm⁻¹ (mid infrared).

When IR radiation interacts with a molecule, it affects vibrational and rotational motions. Absorption occurs when the radiation frequency matches a bond's natural vibration frequency. Molecular vibrations are of two types:

- Stretching vibration: Periodic movement along the bond axis, altering interatomic distance.
- Angular deformation: Change in the angle between two adjacent bonds.

These vibrations produce distinct absorption bands, which are recorded as an "FTIR spectrum" by comparing incident and transmitted radiation. The spectrum displays absorption bands, with intensities expressed as "transmittance" or "absorbance" versus wavenumber. The spectral data provides:

- Qualitative analysis: Absorption wavelengths correspond to specific chemical groups.
- Quantitative analysis: Absorption intensity relates to the concentration of the absorbing group.

Thus, a material's unique absorption bands enable its identification.

In "perovskite structures", IR spectroscopy reveals cation-oxygen vibrational frequencies, influenced by cation mass, bond geometry, and lattice parameters.

The method used for powder preparation is the pellet method, which consists of mixing 1 mg of the sample to be studied with 200 mg of Potassium Bromide KBr (200 mg KBr /

1 mg powder) and then compressing under high pressure to form a pellet. These pellets are dried in an oven overnight before analysis.

The experimental device used in this work is a PerkinElmer spectrum two instrument, Shown in the Figure II.5.



Figure II.5. PerkinElmer spectrum two instrument.

II.1.4. UV-Visible Spectroscopy:

II.1.4.1. General Principle:

UV-Visible absorption spectroscopy is a widely used technique for analyzing the optical properties of materials. It involves measuring the absorption of light in the ultraviolet (200–400 nm) and visible (400–800 nm) spectral regions. In this range, absorption primarily occurs due to electronic transitions from the valence band to the conduction band[7].

In this work, we used the "Evolution 220" UV-Visible spectrophotometer from Thermo Fisher Scientific (shown in Figure II.6). This is a double-beam recording spectrophotometer, equipped with two light sources: a deuterium lamp for the UV region and a halogen lamp for the visible region. The instrument includes a monochromator to select specific wavelengths and an optical system that splits the beam, one part passes through the sample, and the other through a reference. The detector then compares both beams and records the transmittance $T(\lambda)$, as a function of wavelength λ [7].

From the recorded spectra, key optical parameters such as the absorption coefficient (α) and the optical band gap energy (E_g) can be extracted.

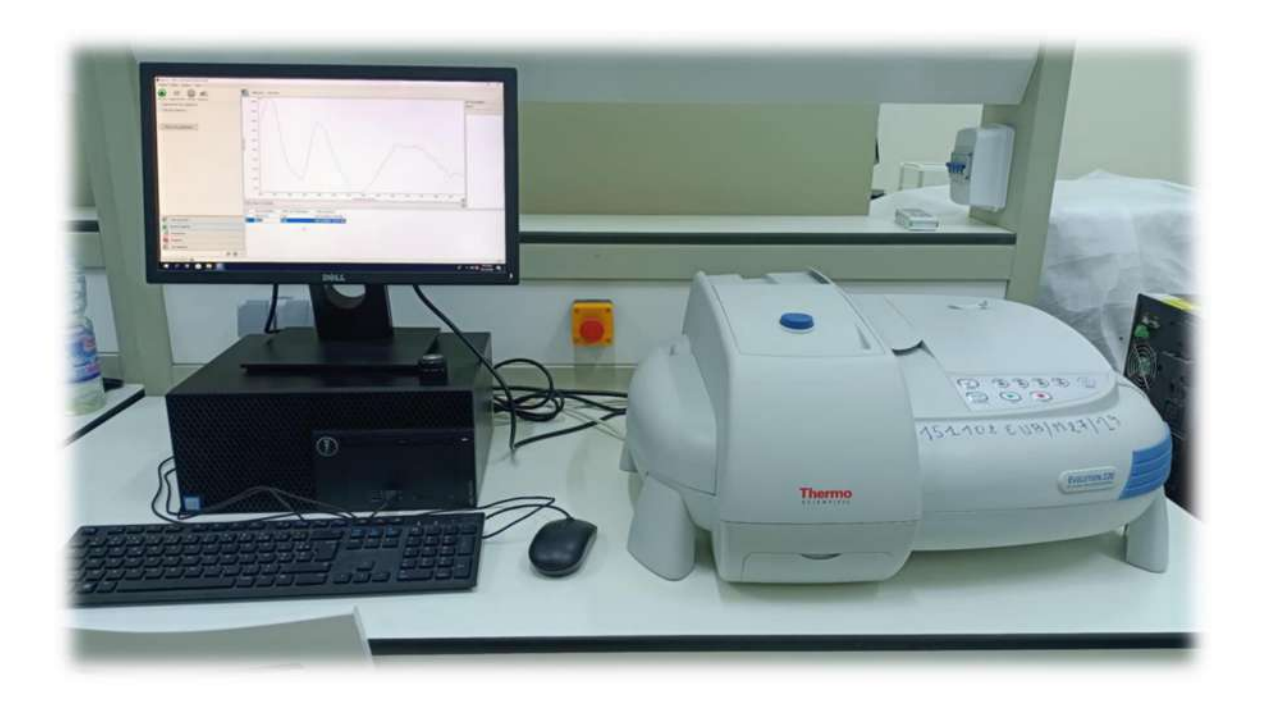


Figure II.6. Evolution 220 UV-Visible spectrophotometer instrument.

II.1.4.2. Absorption Coefficient (α):

The absorption coefficient (α) is a fundamental optical parameter that quantifies how strongly a material absorbs light at a given wavelength. It represents the fraction of incident light absorbed per unit distance as it travels through the material.

The transmittance T is defined as the ratio of the transmitted light intensity I to the incident intensity I_0 , and follows Beer-Lambert's law[8]:

$$T = \frac{I}{I_0} = e^{-\alpha l}$$

Where:

> T: The transmittance (Without unit).

 \triangleright I: The transmitted light intensity (W/m²).

 $ightharpoonup I_0$: The incident intensity (W/m²).

 \triangleright a: is the absorption coefficient (cm⁻¹).

> 1: is the sample thickness (cm).

When T is expressed in percentage (%), the absorption coefficient can be calculated as:

$$\alpha = \frac{1}{l} \ln \left(\frac{100}{T\%} \right)$$

Given the sample thickness l, we can determine $\alpha(\lambda)$ at each wavelength. High α values indicate strong absorption, while a low values indicate transparency or weak absorption.

II.1.4.3. Optical Band Gap (Eg):

The optical band gap (E_g) represents the minimum photon energy required to excite an electron from the valence band to the conduction band. It can be determined experimentally from the absorption coefficient using Tauc's relation, which depends on the nature of the electronic transition[9].

The general form of Tauc's equation is[10]:

$$(\alpha h v)^n = A(h v - E_{\sigma})$$

Where:

> hv: The photon energy (eV).

➤ E_g: Optical band gap energy (eV).

A: A constant.

> n: An exponent that depends on the nature of the transition.

Also, the photon energy is related to the wavelength λ by:

$$hv = \frac{hc}{\lambda} = \frac{1241.25}{\lambda(nm)}$$

> c: Speed of light in vacuum $(3 \times 10^8 \text{ m/s})$.

► h: Planck's constant $(6.626 \times 10^{-34} \text{ J} \cdot \text{s})$.

There are two types of band gaps: direct and indirect. In a direct band gap material, the maximum of the valence band and the minimum of the conduction band occur at the same momentum (k-vector). In an indirect band gap material, the valence band maximum and the conduction band minimum occur at different momenta. This is illustrated in Figure II.7, which shows a schematic comparison between direct and indirect band gap transitions.

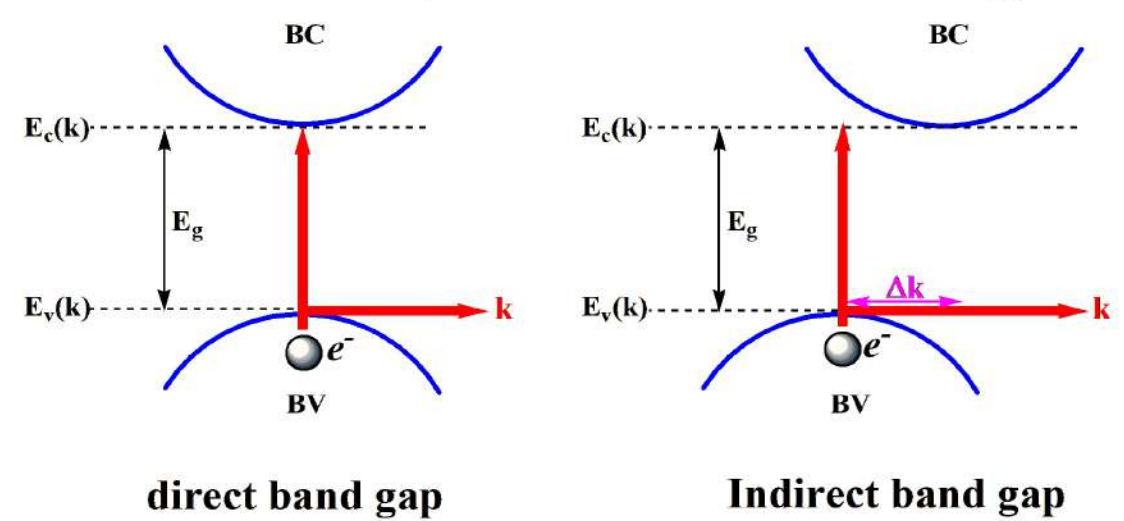


Figure II.7. Comparison between direct and indirect band gap.

For direct band gaps, the electron absorbs a photon and transitions directly from the valence band to the conduction band without any change in momentum. Such transitions are highly efficient and result in strong optical absorption, making direct band gap materials ideal for optoelectronic applications such as light-emitting diodes (LEDs) and laser diodes.

In contrast, for indirect band gaps, an electron transition requires the involvement of both a photon and a phonon (a lattice vibration) to conserve momentum. This additional requirement makes the transition process less efficient, leading to weaker and more gradual absorption near the band edge.

The band gap value is determined (either direct or indirect) by plotting the curve $(\alpha h \nu)^n$ as a function of the photon energy hv [10], where:

- \triangleright (n = 2) for the direct band gap.
- $ightharpoonup (n = \frac{1}{2})$ for the indirect band gap.

By drawing the tangent, we can determine the band gap value, which corresponds to the intersection of the tangent with the photon energy axis at $(\alpha h \nu)^n = 0$ [10].

This analysis allows us to evaluate whether the material exhibits a direct or indirect optical transition, depending on which plot provides the best linear fit in the high-absorption region.

II.2. Computational code and methods:

The properties of materials such as strength, color, conductivity, and magnetism, originate from their atomic arrangements and the behavior of electrons. Therefore, investigating materials at the atomic and subatomic levels is essential for advancements in modern science and engineering. A deep understanding of atomic structures and interactions enables the prediction and design of materials with tailored properties, thereby driving innovation across various technological and industrial fields.

Quantum theory provides the fundamental framework for studying the microscopic structure of matter, with a particular focus on electron behavior, which determines bonding, stability, and interactions [11, 12]. Central to this theory is the Schrödinger equation, whose complexity ranges from simple atoms to complex molecules and solids. Notably, the equation has an exact solution only for the hydrogen atom and its isotopes; for multi-electron systems, approximate solutions are required [13]. To manage this complexity, several simplifications are commonly employed, including the use of atomic units, linear combinations of atomic orbitals, and approximations such as the Born-Oppenheimer and independent electron models [14].

Density Functional Theory (DFT) has emerged as one of the most powerful and widely used methods for solving the many-body Schrödinger equation. It offers an effective compromise between computational efficiency and accuracy, making it the preferred approach in quantum materials modeling.

II.2.1. Density Functional Theory:

DFT is founded on two fundamental theorems proposed by Hohenberg and Kohn, which establish a relationship between the ground-state properties of a system and its electron density.

II.2.1.1. Kohn-Hohenberg first theorem:

"The ground-state energy for Schrodinger equation is a functional of electron density"[15].

A functional is a higher-order function, it's "a function of a function". It takes another function as input and returns a scalar value. Mathematically, it is represented as: F[f(x)]

According to the first Hohenberg-Kohn theorem, the ground-state energy E of a system can be expressed as $E[\rho(r)]$, where $\rho(r)$ is the electron density. This foundational concept is what gives Density Functional Theory its name.

Electron Density $\rho(r)$ is a function that describes the distribution of electrons in space. It represents the probability of finding an electron within a small volume around r [15].

$$\rho(r) = \sum_{i=1}^N |\psi_i(r)|^2$$

Where ψ are the Kohn-Sham orbitals.

This theorem is significant because it allows the complex problem of solving the many-body Schrödinger equation, which involves a wavefunction dependent on 3N variables (for N electrons), to be reduced to a problem involving only three spatial variables—those of the electron density.

II.2.1.2. Kohn-Hohenberg second theorem:

Also known as the Variational Principle, the second theorem states: "The electron density that minimizes the energy of the energy functional is the true ground-state electron density of the system" [15].

In other words, among all possible electron densities, the correct ground-state density is the one that yields the minimum energy when plugged into the energy functional.

We can summarize the two theorems in a simple way: the first theorem confirms that there is a relationship between the energy of the system and the electron density (The ground state energy is a functional of electron density), the second theorem provides a way to calculate this density.

II.2.1.3. Exchange-Correlation Functional:

In multi-electron systems, electrons repel each other, making their paths uncertain. This electron-electron interaction is a major challenge in quantum systems. In DFT, this interaction is captured through the exchange-correlation (XC) functional, which combines exchange (due to the Pauli principle) and correlation (from electron-electron repulsion) energies[14]:

$$E_{XC}[\rho(r)] = E_X[\rho(r)] + E_C[\rho(r)]$$

Since the exact form of the XC functional is unknown, many approximations have been developed. The accuracy of a DFT calculation largely depends on the choice of XC functional, and improving these approximations remains an active area of research.

II.2.1.3.1. The local density approximation (LDA):

The Local Density Approximation (LDA) assumes that the exchange-correlation energy at a given point depends only on the local electron density, as in a uniform electron gas. In this model, the system is treated as composed of many small, homogeneous regions.

The exchange energy E_X of the electron gas can be expressed as [14]:

$$E_X = -\frac{3}{4} (\frac{3}{\pi})^{\frac{1}{3}} \int \rho(r)^{\frac{4}{3}} d^3r$$

For the correlation energy, empirical models are typically employed. A commonly used LDA model is the Perdew-Wang (PW91) functional[16], based on extensive studies of the uniform electron gas:

$$E_{\rm C} = -\frac{3}{10} \left(\frac{3}{\pi}\right)^{\frac{1}{3}} \int (\rho(r))^{\frac{4}{3}} d^3r$$

While LDA has been widely used due to its simplicity, it tends to perform poorly for systems with rapidly varying electron density, such as molecules, surfaces, and interfaces. It also systematically underestimates the band gaps of semiconductors and insulators.

II.2.1.3.2. Generalized gradient approximation (GGA):

The Generalized Gradient Approximation (GGA) improves upon LDA by considering not only the local electron density $\rho(r)$ but also its spatial gradient $\nabla \rho(r)$. This allows GGA to more accurately describe systems with non-uniform electron distributions [14].

The GGA exchange-correlation energy is given by:

$$E_{XC}[\rho(r)] = \int f[\rho(r), \nabla \rho(r)] d^3r$$

Here, "f" is a functional that depends on both the density and its gradient. Different GGA functionals use different forms of "f" many of which are empirically parameterized based on accurate quantum mechanical calculations or experimental data.

Some well-known GGA functionals include:

- Perdew-Burke-Ernzerhof (PBE): One of the most widely used GGA functionals, known for its balance between accuracy and computational efficiency[17].
- ➤ BLYP (Becke-Lee-Yang-Parr): A combination of Becke's exchange functional and Lee-Yang-Parr correlation functional, commonly used in molecular systems[18].
- > revPBE/RPBE (Revised PBE): A revised version of the PBE functional that aims to improve performance for certain systems[19].

GGA generally offers better performance than LDA for systems with spatially varying densities. It improves the prediction of molecular geometries, surface properties, and band gaps, though it still underestimates band gaps to some extent. GGA also suffers from limitations in systems with strong electron correlation and is affected by self-interaction errors.

II.2.1.3.3. Hybrid Functionals:

Hybrid functionals aim to improve the accuracy of DFT by incorporating a portion of exact exchange energy calculated using Hartree-Fock (HF) theory into the DFT exchange-correlation functional. The hybrid exchange-correlation energy is expressed as [14]:

$$E_{XC} = E_{XC}^{DFT} + a(E_X^{HF} - E_X^{DFT})$$

Here, a is a mixing coefficient, typically between 0.2 to 0.3, meaning that 20% to 30% of the exact HF exchange is mixed with 70% to 80% of the DFT exchange.

This approach improves the description of a wide range of properties, including reaction energies, molecular orbitals, and especially band gaps in semiconductors and insulators. However, hybrid functionals are computationally more expensive than GGA or LDA functionals.

II.2.2. Pseudopotential:

In the context of quantum mechanical simulations of materials—particularly within Density Functional Theory (DFT), a pseudopotential is a mathematical construct used to simplify the complex many-body problem of electrons in atoms.

II.2.2.1. Pseudopotential principle:

At the atomic level, electrons are generally classified into two categories: core electrons, which are tightly bound to the nucleus and have minimal impact on chemical bonding, and valence electrons, which are more loosely bound and play a central role in determining the chemical and physical properties of materials.

Accurately modeling core electrons requires a large number of basis functions due to their strong interaction with the nucleus, significantly increasing the computational cost. The pseudopotential method addresses this challenge by replacing the full all-electron potential (which includes both the nucleus and core electrons) with a smoother, effective potential that acts only on the valence electrons. This effective potential retains essential physical features, such as correct scattering behavior and the eigenvalues of occupied states, while eliminating the need to explicitly compute the core electron wavefunctions [20].

By focusing solely on valence electrons, pseudopotentials offer a computationally efficient and robust method for simulating the electronic structure of atoms, molecules, and solids.

II.2.2.2. Pseudopotential types:

Over the years, several types of pseudo-potentials have been developed, each offering different trade-offs in terms of accuracy, efficiency, and computational cost. The most commonly used types include norm-conserving pseudo-potentials, ultrasoft pseudopotentials, and others.

II.2.2.2.1. Norm-Conserving Pseudopotentials (NCPPs):

Norm-conserving pseudopotentials were among the earliest developed and remain widely used due to their reliability and transferability. The defining feature of NCPPs is the conservation of the norm of the pseudo-wavefunction within a cutoff radius, ensuring that it matches the norm of the all-electron wavefunction. This constraint preserves the scattering properties and provides good transferability across different chemical environments. However, norm-conserving pseudopotentials tend to be relatively "hard," requiring a higher plane-wave energy cutoff, which increases computational cost [21].

II.2.2.2.2. Ultrasoft Pseudopotentials (USPPs):

To reduce the computational demands of norm-conserving pseudopotentials, ultrasoft pseudopotentials were introduced by Vanderbilt. These pseudopotentials relax the norm-conservation condition, allowing for smoother (or "softer") pseudo-wavefunctions. As a result, USPPs require significantly lower plane-wave energy cutoffs, making them highly efficient—particularly for systems containing transition metals or elements with semicore states. However, the relaxation of norm conservation necessitates the use of additional augmentation charges to accurately reconstruct the charge density, and the pseudopotentials may be less transferable in some cases [22].

II.2.2.2.3. Other pseudopotential approaches:

Several advanced pseudopotential methods have been developed, such as the projector augmented-wave (PAW) method and all-electron approaches like the full-potential linearized augmented plane wave (FLAPW) method. These techniques are highly accurate, particularly for systems involving localized electrons. However, they are not implemented in CASTEP.

We focus exclusively on norm-conserving and ultra-soft pseudo-potentials, which are natively supported by the CASTEP code and provide a good compromise between accuracy and computational cost.

In practice, many DFT packages provide libraries of pre-generated pseudopotentials. Alternatively, CASTEP supports on-the-fly generation (OTFG), allowing pseudopotentials, either norm-conserving or ultrasoft, to be dynamically generated during a calculation based on user-defined parameters.

II.2.3. Calculation code:

A wide range of computational codes based on Density Functional Theory (DFT) is available, including VASP, ABINIT, CRYSTAL, BigDFT, and CASTEP [23-25].

Among these, CASTEP (Cambridge Serial Total Energy Package) stands out as a comprehensive and versatile DFT code designed to calculate a wide array of physical properties of materials from first principles. Its foundation lies in the accurate computation of total energy, from which many other physical quantities can be derived [25].

While CASTEP primarily focuses on calculating the electronic structure and related properties, the extraction of meaningful insights from these results often requires the use of post-processing tools for visualization and data analysis. Additionally, auxiliary tools that assist in generating accurate input files enhance the usability and flexibility of the code [26].

CASTEP employs the plane-wave pseudopotential method to solve the one-electron Kohn—Sham equations. The wavefunctions are expanded in a plane-wave basis set, defined using periodic boundary conditions and Bloch's theorem. The electron—ion interaction is described using ab initio pseudopotentials, which can be either norm-conserving or ultrasoft.

To obtain the Kohn-Sham wavefunctions and the corresponding charge density selfconsistently, CASTEP utilizes direct energy minimization schemes, particularly the conjugate gradient and density mixing methods. For systems with partial occupancies (such as metals), a robust ensemble DFT approach is employed.

The convergence of CASTEP calculations is primarily governed by two key parameters: the plane-wave energy cutoff, which determines the size of the basis set, and the Brillouin zone sampling, which is controlled by the number of special k-points.

CASTEP has been successfully applied to the study of crystal structures, mechanical properties, and phase stability of various inorganic materials. Although its use in predicting and interpreting spectroscopic properties is promising, such applications are less frequently reported.

In summary, the CASTEP module facilitates first-principles quantum mechanical calculations for exploring the properties of crystalline solids and surfaces, making it a powerful tool in solid-state physics and materials science.

II.2.4. Properties:

II.2.4.1. Structural properties:

The investigation of structural properties is fundamental for understanding the stability and geometry of materials at the atomic scale. In first-principles calculations based on Density Functional Theory (DFT), structural optimization is performed by minimizing the total energy of the system with respect to atomic positions and lattice parameters.

However, prior to any structural relaxation, it is essential to ensure the convergence of computational parameters to achieve accurate and reliable results.

II.2.4.1.1. Convergence Tests:

To ensure reliable structural optimization, convergence tests must be conducted to determine suitable values for the "cutoff energy" (which controls the precision of the plane-wave basis set) and the "k-point mesh density" (which governs Brillouin zone sampling). An inadequately converged setup can lead to significant errors in the calculated properties, while overly strict settings may lead to unnecessary computational expense.

The convergence behavior is assessed by monitoring the equilibrium unit cell volume as a function of increasing cutoff energy and k-point density. The percentage deviation in volume between successive configurations is calculated using the following relation:

$$\Delta V(\%) = \frac{|V_{\rm f} - V_{\rm o}|}{V_{\rm o}} \times 100$$

A well-converged calculation is indicated when ΔV becomes sufficiently small—typically below 1%—beyond which increasing the cutoff energy or k-point density has a negligible effect on the structural parameters. By selecting the lowest values of cutoff energy and k-point mesh that yield this stability, computational cost can be minimized without compromising accuracy.

II.2.4.1.2. Structural Optimization:

Once convergence is confirmed, structural relaxation is performed by minimizing the total energy with respect to atomic positions and lattice constants. The optimized geometry corresponds to the equilibrium configuration of the system, characterized by minimum total energy and vanishing net forces on atoms.

This procedure yields critical structural information, including the equilibrium lattice parameters, atomic coordinates, bond lengths and angles, and unit cell volume.

The optimized structure serves as the foundation for the evaluation of additional physical properties, such as electronic, mechanical, and optical characteristics. Accurate structural optimization is therefore essential to ensure the validity of all subsequent theoretical predictions.

II.2.4.2. Electronic properties:

The study of electronic properties is essential for understanding a material's behavior, as it provides insights into how electrons move and interact within the material, thereby influencing its electrical and optical characteristics [26]. It also allows for the analysis of the nature of the electronic bands formed by interactions between the constituent elements [27].

In solid-state physics, the analysis of electronic properties typically focuses on the band structure and the density of states (DOS).

II.2.4.2.1. The Brillouin zone:

In electronic structure calculations, the Brillouin zone (BZ) represents the fundamental region in reciprocal space, reflecting the symmetry of the underlying crystal lattice. The electronic band structure is computed along selected high-symmetry paths within the first Brillouin zone to capture significant transitions and dispersion features.

In this study, the band structure was calculated along the path connecting the high-symmetry k-points Z-Γ-Y-A-B-D-E-C, as defined by the monoclinic lattice. These directions allow for a detailed analysis of the conduction and valence bands, enabling the identification of the bandgap type, bandwidth, and effective mass of charge carriers.

Understanding the electronic dispersion along these paths provides key insights into the material's electronic performance and its potential for optoelectronic applications.

II.2.4.2.2. Band structure:

The band structure of a material describes the allowed and forbidden energy levels for electrons and is fundamental in determining whether the material behaves as a metal, semiconductor, or insulator. In perovskite materials, the band structure is influenced by atomic composition, crystal symmetry, and electronic interactions.

If the valence band maximum (VBM) and conduction band minimum (CBM) occur at the same wave vector k, the material exhibits a direct band gap. Conversely, if the VBM and CBM are located at different k-points, the material has an indirect band gap[27].

II.2.4.2.3. Density of state:

To gain a deeper understanding of the electronic structure, the density of states (DOS) is analyzed. The DOS provides valuable information about the atomic and orbital origins of electronic states within the band structure.

A comprehensive analysis includes both the total density of states (TDOS) and the partial density of states (PDOS). The TDOS indicates the number of electronic states per unit energy across the system, while the PDOS reveals the contributions of individual atoms and their orbitals (e.g., s, p, d) to specific energy levels [26].

The PDOS is obtained by decomposing the TDOS into contributions from the atomic orbitals of each constituent atom. It is important to note that the Fermi level is set at 0 eV for reference [27].

II.2.4.3. Optical properties:

Optical properties describe how a material interacts with electromagnetic radiation and visible light. These characteristics are essential for analyzing the optical spectra, which are closely related to the electronic structure and are critical for evaluating the composition and optoelectronic behavior of materials.

II.2.4.3.1. Dielectric function:

The dielectric function $\varepsilon(\omega)$ is fundamental to the study of optical properties, as it characterizes the material's response to an external electromagnetic field:

$$\varepsilon(\omega) = \varepsilon_1(\omega) + i\varepsilon_2(\omega).$$

Here, $\varepsilon_1(\omega)$ is the real part, representing the material's ability to store energy from the field, and $\varepsilon_2(\omega)$ is the imaginary part, associated with the energy dissipation due to interband electronic transitions[28].

II.2.4.3.2. Reflectivity:

Reflectivity indicates the fraction of incident light reflected by the surface of a material. It is calculated using the dielectric function as follows:

$$R(\omega) = \left| \frac{\sqrt{\epsilon_1(\omega) + i\epsilon_2(\omega)} - 1}{\sqrt{\epsilon_1(\omega) + i\epsilon_2(\omega)} + 1} \right|^2$$

This parameter is crucial for assessing the optical response of a material, particularly at different photon energies.

II.2.4.3.3. Refractive index and extinction coefficient:

The refractive index (n) and extinction coefficient (k) describe how light propagates through and is absorbed by a material[29, 30]. When the refractive index becomes complex, it is expressed as:

$$N = n(\omega) - ik(\omega)$$

The real part $n(\omega)$ describes the bending of light, while the imaginary part $k(\omega)$ corresponds to the attenuation of the wave (i.e., absorption). They are calculated from the dielectric function using the following relations:

$$n(\omega) = \sqrt{\frac{\sqrt{\epsilon_1^2(\omega) + \epsilon_2^2(\omega)} + \epsilon_1(\omega)}{2}}$$

$$k(\omega) = \sqrt{\frac{\sqrt{\epsilon_1^2(\omega) + \epsilon_2^2(\omega)} - \epsilon_1(\omega)}{2}}$$

The refractive index governs how much light is refracted, while $k(\omega)$ interprets the absorption of the electromagnetic wave as it travels through the material [29].

II.2.4.3.4. Absorption coefficient:

The absorption coefficient $\alpha(\omega)$ quantifies the amount of energy absorbed per unit distance as the wave propagates through the material. It is expressed as:

$$\alpha(\omega) = \frac{4\pi}{\lambda} k(\omega)$$

Where λ is the wavelength of the incident light in vacuum. A high $\alpha(\omega)$ value indicates strong absorption, which is important in optoelectronic applications.

II.2.4.3.5. Optical conductivity:

Optical conductivity (or photoconductivity) reflects how the material conducts electric current under photon excitation. It arises from electronic transitions between occupied and unoccupied states, especially across the bandgap. It can be calculated from the dielectric function using:

$$\sigma(\omega) = -\frac{\mathrm{i}\omega}{4\pi} \; \epsilon(\omega)$$

This parameter provides key insights into how efficiently the material responds to optical excitation.

II.2.4.3.6. The energy loss function:

The energy loss function $L(\omega)$ is essential for understanding how high-energy electrons lose energy as they pass through a material. It is defined as:

$$L(\omega) = \frac{\epsilon_2(\omega)}{\epsilon_1^2(\omega) + \epsilon_2^2(\omega)}$$

This function reveals the energy loss mechanisms and is particularly useful in identifying the bulk plasma frequency, which corresponds to the peak of $L(\omega)$. This peak typically occurs when:

$$\epsilon_1(\omega) = 0$$
 $\epsilon_2(\omega) < 1$

II.2.4.4. Mechanical properties:

The study of mechanical properties is a critical aspect of materials science. Properties such as elastic anisotropy, mechanical stability, and the ductile or brittle nature of materials are directly related to their elastic constants. These moduli are essential for a wide range of engineering applications in which materials are subjected to mechanical stresses.

Key mechanical parameters, namely, the bulk modulus (B), shear modulus (G), Young's modulus (E), and Poisson's ratio (v), provide insight into how a material responds to external forces and deformations. They are crucial for understanding structural stability and the nature of atomic bonding.

The elastic constants of solids connect their mechanical and dynamic behavior, offering essential information about their stability and stiffness. Generally, isotropic elastic moduli cannot be directly obtained from ab initio calculations. Instead, these parameters must be derived from the single-crystal elastic constants, Cij.

The compounds under study crystallize in the monoclinic system, which possesses 13 independent elastic constants: C_{11} , C_{22} , C_{33} , C_{44} , C_{55} , C_{66} , C_{12} , C_{13} , C_{23} , C_{15} , C_{25} , C_{35} and C_{46} . The calculation of these constants is sufficient to describe the mechanical properties of the material.

For mechanical stability in a monoclinic crystal system, a necessary and sufficient condition is that all eigenvalues of the elastic stiffness matrix C be positive. This condition can be verified using standard linear algebra routines[31]. The eigenvalues λ are obtained by solving the characteristic polynomial:

$$det(C - \lambda I) = 0$$

Where "det" signifies the determinant of the matrix, "C" is the elastic stiffness matrix, λ represent the eigenvalues of the matrix, and "I" is the identity matrix.

Since the matrix C is a symmetric 6×6 matrix, this yields six real eigenvalues. Mechanical stability is guaranteed only if all eigenvalues are strictly positive.

II.2.4.4.1. Bulk Modulus (B):

The bulk modulus B represents a material's resistance to uniform compression and correlates with the bond strength among atoms in the crystal. It serves as a benchmark for assessing average bond strength. For monoclinic crystals, B is calculated from elastic constants using:

- ightharpoonup The Voigt approximation: $B_v = \frac{1}{9}[C_{11} + C_{22} + C_{33} + 2(C_{12} + C_{13} + C_{23})]$
- The Reuss approximation: $B_R = [S_{11} + S_{22} + S_{33} + 2(S_{12} + S_{13} + S_{23})]^{-1}$

Where S_{ij} are the elastic compliance constants, obtained by inverting the stiffness matrix.

➤ Hill approximation (arithmetic mean of Voigt and Reuss):

$$B_{H} = \frac{B_{v} + B_{R}}{2}$$

II.2.4.4.2. Shear Modulus (G):

The shear modulus G quantifies a material's resistance to shape deformation (shear). It is derived as follows:

> The Voigt approximation:

$$G_{v} = \frac{1}{15} [C_{11} + C_{22} + C_{33} + 3(C_{44} + C_{55} + C_{66}) - (C_{12} + C_{13} + C_{23})]$$

> The Reuss approximation:

$$\frac{1}{G_{P}} = \frac{4}{15}(S_{11} + S_{22} + S_{33}) - \frac{4}{15}(S_{12} + S_{13} + S_{23}) + \frac{1}{5}(S_{44} + S_{55} + S_{66})$$

➤ Hill approximation:

$$G_{\rm H} = \frac{G_{\rm v} + G_{\rm R}}{2}$$

II.2.4.4.3. The Young's modulus (E):

Young's modulus E characterizes the material's stiffness under uniaxial tension or compression. It depends on bond strength and material structure (amorphous or crystalline). It is computed using:

$$E = \frac{9B_HG_H}{G_H + 3B_H}$$

Higher values of E indicate greater stiffness and resistance to elongation or compression.

II.2.4.4.4. Poisson's Ratio (v):

Poisson's ratio v reflects the nature of interatomic bonding forces and is calculated as:

$$\nu = \frac{(3B_{H} - 2G_{H})}{2(3B_{H} + G_{H})}$$

Typically, covalent materials exhibit low Poisson's ratios ($\nu \approx 0.1$), while ionic materials show higher values. According to Nye, a value of $0.25 < \nu < 0.50$ indicates the presence of central interatomic forces. A material is generally considered ductile if $\nu > 0.26$, and brittle if $\nu \leq 0.26$ [32].

II.2.4.4.5. Pugh's ratio (B/G):

Pugh's ratio B/G is an empirical parameter used to predict ductility. A value greater than 1.75 suggests ductile behavior, while values below 1.75 indicate brittleness [32].

II.2.4.4.6. Universal anisotropy index (AU):

The universal elastic anisotropy index A^U quantifies the directional dependence of elastic properties and is given by [33]:

$$A^{U} = \frac{B_{V}}{B_{R}} + 5\frac{G_{V}}{G_{R}} - 6$$

A value of zero indicates isotropic behavior, while nonzero values indicate elastic anisotropy.

II.2.4.4.7. Debye temperature (θ_D) :

The Debye temperature (θ_D) is a fundamental parameter associated with thermal properties, such as specific heat, thermal expansion, and melting point. It is defined as[34]:

$$\theta_{\rm D} = \frac{h}{k_{\rm B}} \left[\frac{3n}{4\pi} \left(\frac{N_{\rm A}}{M} \rho \right) \right]^{\frac{1}{3}} \times v_{\rm m}$$

In the above equation, n signifies the number of atoms in a molecule, ρ denotes the density of the solid, N_A represents Avogadro's number, M represents the molecular weight, h represents Planck's constant, k_B denotes Boltzmann's constant, and v_m represents the average speed of sound in a given medium, and can be determined as[34]:

$$v_{\rm m} = \left[\frac{1}{3} \left(\frac{2}{v_{\rm t}^3} + \frac{1}{v_{\rm l}^3}\right)\right]^{-\frac{1}{3}}$$

Where v_t represents the transverse wave velocity, and v_1 is the longitudinal wave velocity. These can be calculated using the elastic moduli and density as follows [34]:

$$v_1 = \left(\frac{3B + 4G}{3\rho}\right)^{\frac{1}{2}}$$

$$v_{\rm t} = \left(\frac{\rm G}{\rho}\right)^{\frac{1}{2}}$$

A higher Debye temperature θ_D implies stronger interatomic bonds and higher stiffness. Lower values are associated with more easily deformable materials due to weaker bonding.

II.2.4.5. Phonon:

Phonons are typically used to evaluate the dynamic stability of a crystal structure. In solid-state physics, a phonon represents the collective excitation of atoms in a periodic lattice, propagating similarly to sound waves. It is also considered the quantum of lattice vibrational energy [35]. A structure is dynamically stable when no soft modes (i.e., negative frequencies) appear in the phonon dispersion; otherwise, it is deemed unstable.

Bibliographic references:

- [1] N.F. Atta, A. Galal, E.H. El-Ads, Perovskite nanomaterials—synthesis, characterization, and applications, Article, Perovskite Materials-Synthesis, Characterisation, Properties, and Applications, 1 (2016).
- [2] Y. Xu, Ferroelectric materials and their applications, Book, Elsevier (2013).
- [3] G. Berti, R. Delhez, S. Norval, B. Peplinski, E. Tolle, J. Verollet, Standardisation of X-ray powder diffraction methods, Conference, Materials Science Forum (2004).
- [4] C.V. Stan, C.M. Beavers, M. Kunz, N. Tamura, X-ray diffraction under extreme conditions at the Advanced Light Source, Article, Quantum Beam Science, 2 (2018).
- [5] Y. Waseda, E. Matsubara, K. Shinoda, X-ray diffraction crystallography: introduction, examples and solved problems, Book, Springer Science & Business Media (2011).
- [6] A.A. Bunaciu, E.G. UdriŞTioiu, H.Y. Aboul-Enein, X-ray diffraction: instrumentation and applications, Article, Critical reviews in analytical chemistry, 45 (2015).
- [7] H.-H. Perkampus, UV-VIS Spectroscopy and its Applications, Book, Springer Science & Business Media (2013).
- [8] G. Lothian, Beer's law and its use in analysis. A review, Article, Analyst, 88 (1963).
- [9] A. Chovet, P. Masson, Physique des semi-conducteurs, Article, Université d'école polytechnique de Marseille, (2004).
- [10] J. Klein, L. Kampermann, B. Mockenhaupt, M. Behrens, J. Strunk, G. Bacher, Limitations of the Tauc plot method, Article, Advanced Functional Materials, 33 (2023).
- [11] A. Beiser, Concepts of modern physics, Book, McGraw-Hill (2003).
- [12] S.T. Thornton, A.F. Rex, C.E. Hood, Modern physics for scientists and engineers, Book, Saunders College Pub (2000).
- [13] I.N. Levine, D.H. Busch, H. Shull, Quantum chemistry, Book, Pearson Prentice Hall Upper Saddle River (2009).
- [14] V. Gupta, Principles and applications of quantum chemistry, Book, Academic Press (2015).
- [15] W. Koch, M.C. Holthausen, A chemist's guide to density functional theory, Book, John Wiley & Sons (2015).
- [16] J.P. Perdew, Y. Wang, Accurate and simple analytic representation of the electron-gas correlation energy, Article, Physical Review B, 45 (1992).
- [17] M. Ernzerhof, G.E. Scuseria, Assessment of the Perdew-Burke-Ernzerhof exchange-correlation functional, Article, The Journal of chemical physics, 110 (1999).
- [18] P.M. Gill, B.G. Johnson, J.A. Pople, M.J. Frisch, The performance of the Becke—Lee—Yang—Parr (B—LYP) density functional theory with various basis sets, Article, Chemical Physics Letters, 197 (1992).
- [19] B. Hammer, L.B. Hansen, J.K. Nørskov, Improved adsorption energetics within density-functional theory using revised Perdew-Burke-Ernzerhof functionals, Article, Physical Review B, 59 (1999).

- [20] B.J. Austin, V. Heine, L.J. Sham, General theory of pseudopotentials, Article, Physical Review, 127 (1962).
- [21] D. Hamann, M. Schlüter, C. Chiang, Norm-conserving pseudopotentials, Article, Physical review letters, 43 (1979).
- [22] G. Kresse, D. Joubert, From ultrasoft pseudopotentials to the projector augmented-wave method, Article, Physical Review B, 59 (1999).
- [23] J. Hafner, Ab-initio simulations of materials using VASP: Density-functional theory and beyond, Article, Journal of computational chemistry, 29 (2008).
- [24] X. Gonze, J.-M. Beuken, R. Caracas, F. Detraux, M. Fuchs, G.-M. Rignanese, L. Sindic, M. Verstraete, G. Zerah, F. Jollet, First-principles computation of material properties: the ABINIT software project, Article, Computational Materials Science, 25 (2002).
- [25] M. Segall, P.J. Lindan, M.a. Probert, C.J. Pickard, P.J. Hasnip, S. Clark, M. Payne, First-principles simulation: ideas, illustrations and the CASTEPcode, Article, Journal of Physics: Condensed Matter, 14 (2002).
- [26] R. Charif, R. Makhloufi, S.C. Mouna, A. Chadli, A. Barkat, M. Nouiri, Structural, electronic, optical, mechanical, and phononic bulk properties of tetragonal trirutile antimonate MSb2O6 (M= Fe, Co, Ni, or Zn): a first-principles prediction for optoelectronic applications, Article, Physica Scripta, 99 (2024).
- [27] K. Meliani, S. Haireche, Theoretical study of structural, electronic, elastic and optical properties of SrS compound under pressure, Thesis, University Yahia Fares of Medea (2022).
- [28] C. Homes, T. Vogt, S. Shapiro, S. Wakimoto, A. Ramirez, Optical response of high-dielectric-constant perovskite-related oxide, Article, science, 293 (2001).
- [29] S. Singh, Refractive index measurement and its applications, Article, Physica Scripta, 65 (2002).
- [30] R. Adair, L. Chase, S.A. Payne, Nonlinear refractive index of optical crystals, Article, Physical Review B, 39 (1989).
- [31] F. Mouhat, F.-X. Coudert, Necessary and sufficient elastic stability conditions in various crystal systems, Article, Physical Review B, 90 (2014).
- [32] G.N. Greaves, A.L. Greer, R.S. Lakes, T. Rouxel, Poisson's ratio and modern materials, Article, Nature materials, 10 (2011).
- [33] C.M. Kube, Elastic anisotropy of crystals, Article, AIP advances, 6 (2016).
- [34] O.L. Anderson, A simplified method for calculating the Debye temperature from elastic constants, Article, Journal of Physics and Chemistry of Solids, 24 (1963).
- [35] A. Togo, I. Tanaka, First principles phonon calculations in materials science, Article, Scripta Materialia, 108 (2015).

CHAPTER III

Results and Discussions

This chapter outlines the key findings of the present study, combining both experimental investigations and first-principles calculations. It begins with a detailed description of the synthesis process for the studied perovskite compounds, followed by the results of structural and optical characterizations using techniques such as X-ray powder diffraction (XRPD), Fourier-transform infrared spectroscopy (FTIR), and UV-visible spectroscopy. The second part of the chapter focuses on the theoretical analysis carried out using density functional theory (DFT), which includes the evaluation of structural, electronic, optical, and mechanical properties, indicating some probable applications.

III.1. Synthesis and characterisation:

III.1.1. Synthesis steps:

The synthesis of our samples was carried out using the ceramic method (solid-state method), described in detail in Chapter II.

Weighing and mixing:

The quantities of reagents required to synthesize approximately 20 g of each composition were calculated and weighed in stoichiometric proportions corresponding to the desired nominal composition, taking into account the purity of the starting materials.

The first step involves gathering the raw materials required for the synthesis. To obtain a homogeneous mixture, the starting powders are dispersed in a small amount of ethanol and stirred using a magnetic stirrer (Figure III.1) for 2 hours.

Ethanol is chosen due to its low evaporation point, which facilitates drying and ensures it does not react with any component of the mixture.

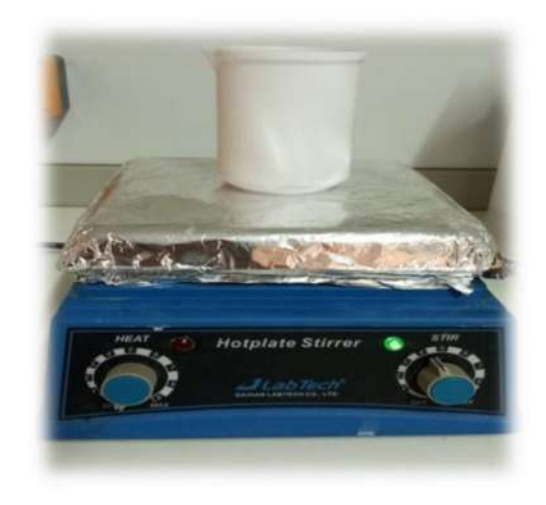


Figure III.1. Magnetic Stirring Setup.

Oven drying:

The mixture is then dried at 90 °C in an oven for 24 hours to remove ethanol and residual moisture (Figure III.2).





Figure III.2. Oven used for drying the powder mixture.

Grinding:

Finally, the powders are ground in a glass mortar for two to three hours (Figure III.3).



Figure III.3. Powder after grinding in a glass mortar.

Calcination:

The heat treatment was carried out in two different programmable furnaces (Nabertherm) under ambient conditions. The temperature was increased at a rate of 2 °C/min until the target temperature was reached and then maintained for several hours. Cooling was performed in open air.

For Compound N°2, the heat treatment was performed at approximately 1200 °C for 60 hours, followed by 1260 °C for 24 hours, and finally 1290 °C for 24 hours, which is considered the reaction temperature.

For Compound N°1, the heat treatment was performed at approximately 1200 °C for 60 hours, then 1260 °C for 24 hours, 1290 °C for 24 hours, 1350 °C for 12 hours, and finally 1430 °C for 24 hours, which is the reaction temperature.

Regrinding:

Processes of regrinding was carried out between each 24 h of calcination process, for one hour.

Shaping:

This involves forming a disc of the materials using a mold and a press. After grinding, the resulting powder is compacted into pellets weighing 1 g and approximately 13 mm in diameter (Figure III.4).



Figure III.4. Pellets of Compound $N^{\circ}1$ and $N^{\circ}2$.

Sintering:

After preparing the pellets of our samples, they are placed in the furnace to perform the process sintering:

- ➤ Compound N°1 was sintered at 1450°C for 6 hours.
- > Compound N°2 was sintered at 1290°C for 12 hours.

| Chapter | III: | Results | and | discussion |
|---------|------|---------|-----|------------|
| Chapter | 111. | Meaning | anu | uiscussivi |

III.1.2.X-ray powder diffraction:

| Chapter | III: | Results | and | discussions |
|---------|------|---------|-----|-------------|
| | - | | | |

| Char | nter | III. | Recult | e and | discussions |
|------|------|------|--------|-------|-------------|
| Спа | JUEL | 111. | resuit | 5 anu | aiscussions |

III.1.3. Fourier Transform Infrared Spectroscopy (FTIR):

| Chapter III | : K | lesults | and | discussions |
|-------------|-----|---------|-----|-------------|
|-------------|-----|---------|-----|-------------|

III.1.4. UV-Visible Spectroscopy:

| Chapter III: Results and discussions | | | | | | |
|--------------------------------------|--|--|--|--|--|--|
| | | | | | | |
| | | | | | | |
| | | | | | | |
| | | | | | | |
| | | | | | | |
| | | | | | | |
| | | | | | | |
| | | | | | | |
| | | | | | | |
| | | | | | | |
| | | | | | | |
| | | | | | | |
| | | | | | | |
| | | | | | | |

III.2. Computational results:

First-principles calculations based on density functional theory (DFT) were carried out using the "Cambridge Serial Total Energy Package" (CASTEP)[3-5] in "Material Studio" [6]. The exchange–correlation effects were described using the generalized gradient approximation (GGA) in Perdew–Burke–Ernzerhof (PBE) formulation.

Ultra-soft pseudopotentials were employed to describe the interactions between ions and electrons. Due to the presence of magnetic elements the compound was optimized and studied using spin-polarized calculations.

III.2.1. Structural properties:

Before investigating the material's properties, geometry optimization was performed to ensure reliable DFT results. The optimization was carried out using a plane-wave cutoff energy of 550 eV and a Monkhorst-Pack k-point grid of $8\times8\times7$, which provided the best convergence behavior. The optimized structures satisfied the following convergence thresholds: an energy convergence of $0.2\times10^{-5} \text{eV/atom}$, a maximum atomic displacement of $0.002\,\text{Å}$, a maximum force of $0.05\,\text{eV/Å}$, and a maximum stress of $0.1\,\text{GPa}$.

Due to the presence of partial occupancies in the crystallographic data, computational models approximate each mixed site using a virtual atom with averaged properties. While this simplifies the modeling process, it may affect the accuracy of predicted physical properties.

To mitigate this, we constructed a $(1\times3\times1)$ supercell by tripling the unit cell along the b-axis. This allowed explicit substitution of different cations at distinct lattice sites, thus eliminating virtual atom artifacts and providing a more realistic atomic arrangement. The resulting lattice parameters are listed in Table III.1.

Table III.1. Supercell lattice parameters of Compound N°1 and Compound N°2 before and after optimization

| Compound | | Compound N°1 | Compound N°2 | |
|--|---------------------|--------------|--------------|--|
| u ₀ | a (Å) | 5.60380 | 5.60380 | |
| izati | b (Å) | 16.79640 | 16.79640 | |
| ptim | c (Å) | 7.91240 | 7.91240 | |
| Before optimization | γ(°) | 90.0000 | 90.0000 | |
| Bef | V (Å ³) | 744.7441 | 744.7441 | |
| u u | a (Å) | 5.69560 | 5.72650 | |
| After optimization | b (Å) | 17.18750 | 17.33560 | |
| ptimi | c (Å) | 7.97530 | 8.09210 | |
| ter 0 | γ(°) | 90.2862 | 90.3050 | |
| Af | V (Å ³) | 780.7173 | 803.3101 | |
| Energy/ | atom (eV/atom) | -685.378315 | -590.9329367 | |
| cohesive energy (eV/atom) -7.957095 -7.746003 | | -7.746003333 | | |

The geometry optimization of the supercell revealed a slight deviation in the γ angle, leading to a transformation of the crystal system from orthorhombic to monoclinic, with the space group P21/m (No. 11). This change suggests that the monoclinic configuration is energetically more stable under the DFT conditions applied.

The cohesive energies of Compound $N^{\circ}1$ and Compound $N^{\circ}2$ were found to be -7.96 eV/atom and -7.75 eV/atom, respectively. The negative values confirm the thermodynamic stability of both compounds. Moreover, the more negative cohesive energy of Compound $N^{\circ}1$ suggests stronger interatomic bonding and enhanced chemical stability compared to Compound $N^{\circ}2$ counterpart.

III.2.2. Electronic properties:

We have computed the band gap and density of states (total and partial) using the optimized supercell. The energy band structure was calculated along high symmetry directions (Z-G-Y-A-B-D-E-C) within the first Brillouin zone using the GGA-PBE functional within the DFT framework.

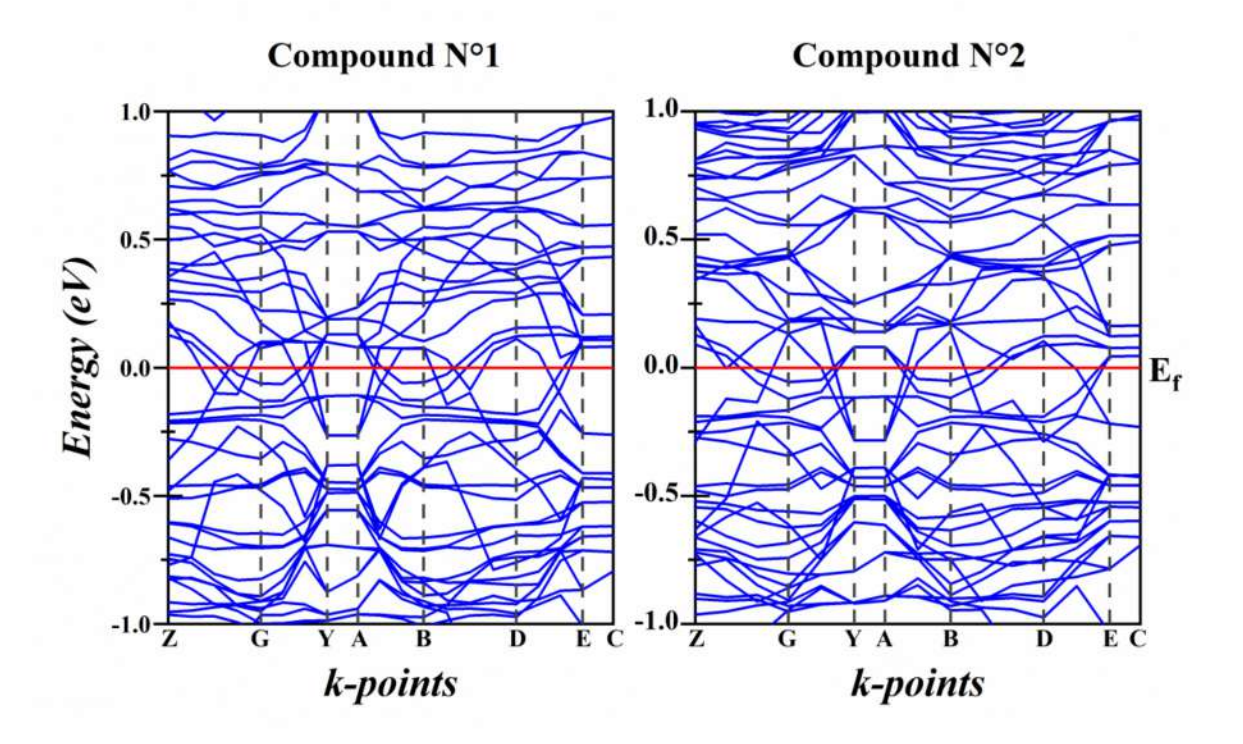


Figure III.12. Band structure of Compound N°1 and Compound N°2.

Figure III.12 illustrates the computed band structures of Compound N°1 and Compound N°2 triple perovskites, where the valence band (VB) and conduction band (CB) are separated by a dashed red line indicating the Fermi level. The band structure calculations for both Compound N°1 and Compound N°2 confirm their metallic behavior. It is observed that there is no forbidden energy band, only an overlap between VB and CB, as electronic bands intersect the Fermi level in each case.

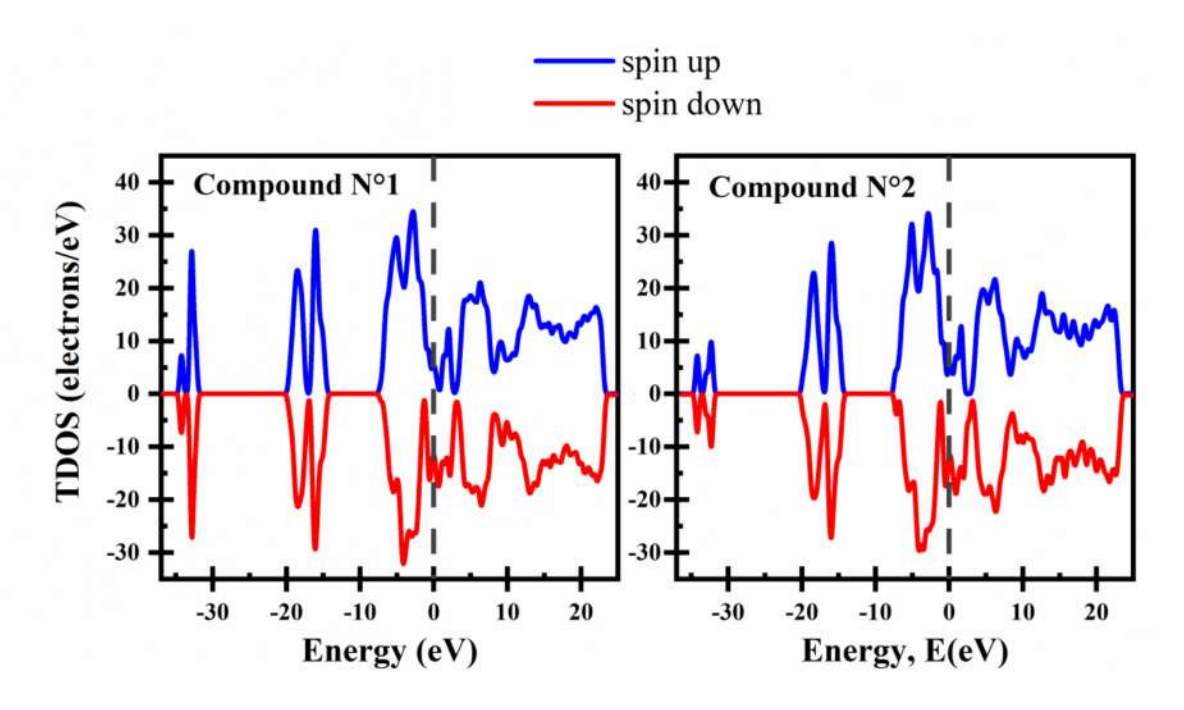


Figure III.13. TDOS of the triple perovskites Compound N°1 and Compound N°2.

The total density of states (TDOS) for both Compound N°1 and Compound N°2 is presented in Figure III.13, within the energy range of −37 eV to 25 eV. The analysis further supports the findings obtained from the band structure. Both compounds exhibit a finite density of states at the Fermi level, confirming their metallic nature. Although the TDOS profiles of the two compounds appear similar near the Fermi level, but this does not negate the presence of slight differences, which may reflect variations in electronic hybridization and bonding environments influenced by the different B-site cations. Notably, the asymmetry observed between the spin-up and spin-down channels indicates the presence of magnetic behavior in both compounds.

III.2.3. Optical Properties:

Optical properties play a crucial role in determining the potential applications of materials in optoelectronics, coatings, and energy-related technologies[7]. The interaction of light with materials is often characterized through various parameters, including the dielectric function, reflectivity, refractive index, extinction coefficient, absorption coefficient, optical conductivity, and energy loss function. These properties provide insights into the electronic transitions and response of the material to electromagnetic radiation.

III.2.3.1. Dielectric Function:

The real and imaginary parts of the dielectric function for Compound N°1 and Compound N°2 are shown in Figure III.14.

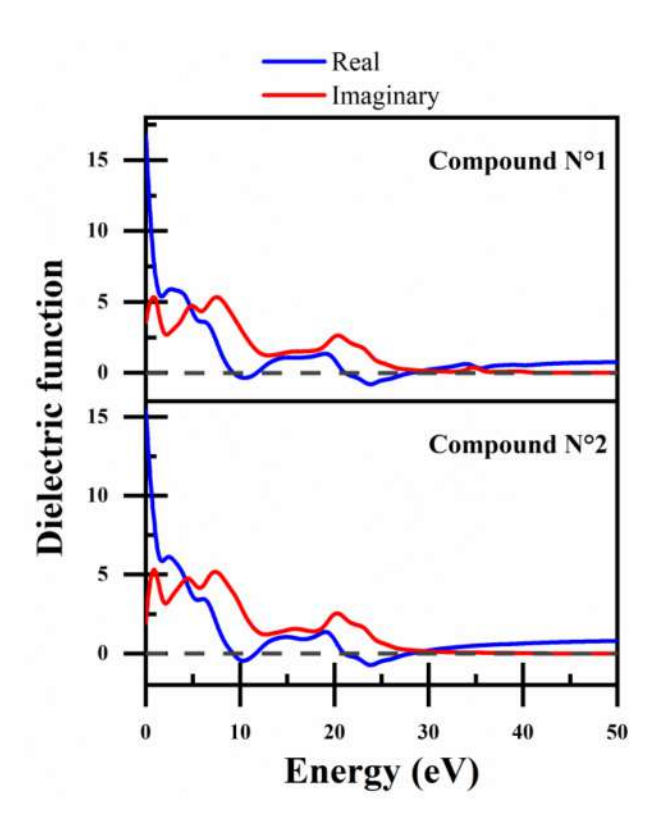


Figure III.14. The dielectric function (real and imaginary part) of Compound N°1 and Compound N°2.

The static dielectric constants $\varepsilon_1(0)$ are 16.7 and 15.4 for the Compound N°1 and Compound N°2, respectively. These relatively high values reflect considerable polarizability in both materials, suggesting strong dielectric screening effects.

The real part of the dielectric function, $\varepsilon_1(0)$, exhibits characteristic zero-crossings at approximately 9 eV and 21 eV, with negative values in the intermediate energy ranges (from 9 to 12 eV and from 21 to 28 eV). This behavior is indicative of screened plasma resonances and suggests metallic-like optical responses within these energy intervals.

The imaginary part, $\varepsilon_2(\omega)$ initiates at non-zero values near 3.4 eV for Compound N°1 and 1.8 eV for Compound N°2. The absence of a sharp onset implies no clear optical band gap, consistent with possible electronic transitions from defect or mid-gap states.

Strong interband transitions are observed, with $\epsilon_2(\omega)$ values ranging between 2 and 6 within 0 to 11 eV energy range, confirming significant optical activity due to valence-to-conduction band transitions.

III.2.3.2. Refractive Index and Extinction Coefficient:

The refractive index (n) and extinction coefficient (k) results of Compound N°1 and Compound N°2 are presented in the graphs shown in Figure III.15.

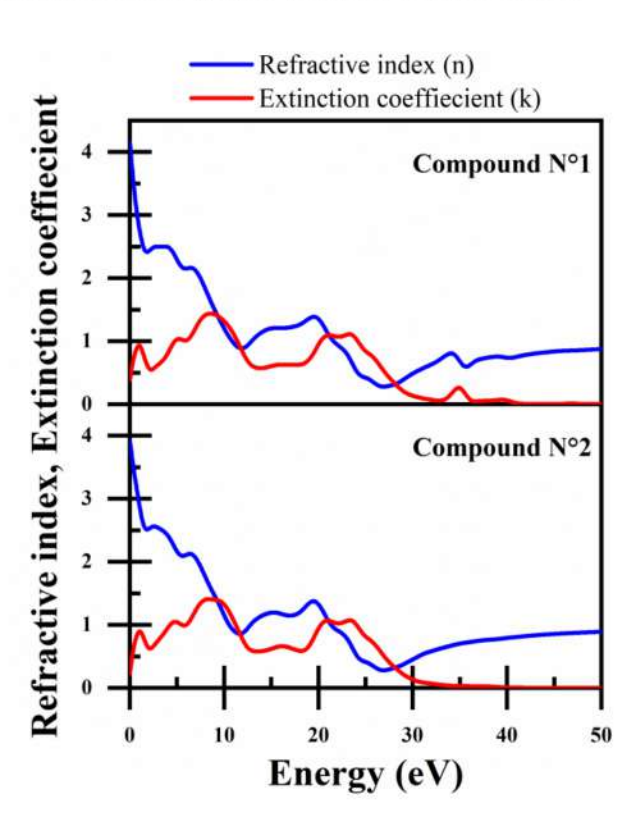


Figure III.15. Refractive index (n) and extinction coefficient (k) of Compound N°1 and Compound N°2.

The refractive index (n) demonstrates high static values of 4.15 for Compound N°1 and 4.00 for Compound N°2. Both compounds maintain ≥ 2 across broad energy ranges up to 7.4 eV (Compound N°1) and 7.2 eV (Compound N°2), indicating sustained high optical density and strong light—matter interaction in the visible to near-UV regions.

The extinction coefficient (k) also supports strong absorption characteristics. At 0 eV, initial k values are 0.34 (Compound N°1) and 0.20 (Compound N°2), with maxima reaching 1.44 at 8.5 eV. Values remain within 0.5 to 1.5 range up to 27 eV, further supporting the interpretation of strong optical absorption in the medium to high-energy range.

III.2.3.3. Reflectivity:

The reflectivity results of Compound N°1 and N°2 are presented in Figure III.16.

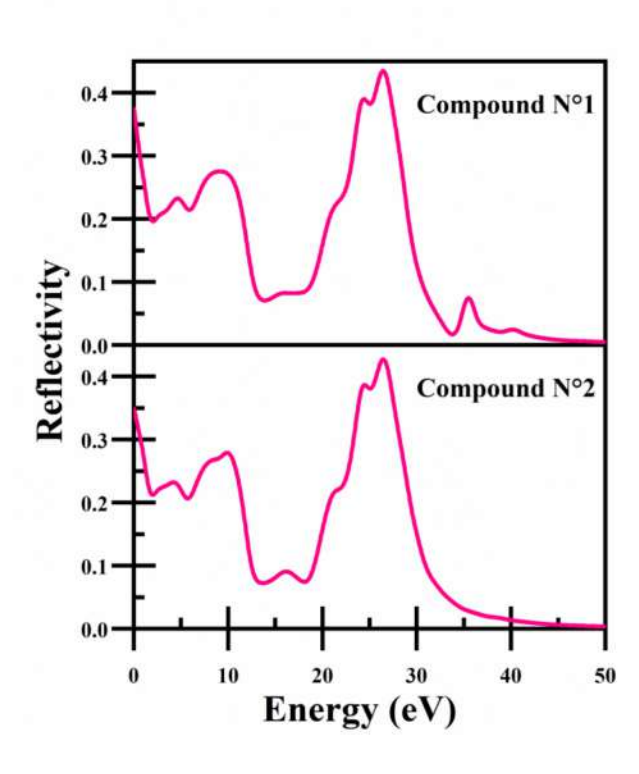


Figure III.16. Reflectivity behavior of Compound N°1 and Compound N°2.

For Compound N°1, the reflectivity $R(\omega)$ starts at 0.38 and peaks at 0.43 around 26.5 eV. Compound N°2 shows slightly lower initial reflectivity at 0.35 but reaches a similar maximum at the same energy. Both compounds maintain significant reflectivity (R > 0.2) within 0 to 11.5 eV and 20.5 to 29 eV energy windows. Reflectivity drops to negligible values beyond 46 eV (Compound N°1) and 44 eV (Compound N°2), indicating reduced optical interaction at very high photon energies and defining their transparency thresholds.

III.2.3.4. Absorption Coefficient:

The absorption coefficient results of Compound N°1 and N°2 are presented as graphs in Figure III.17.

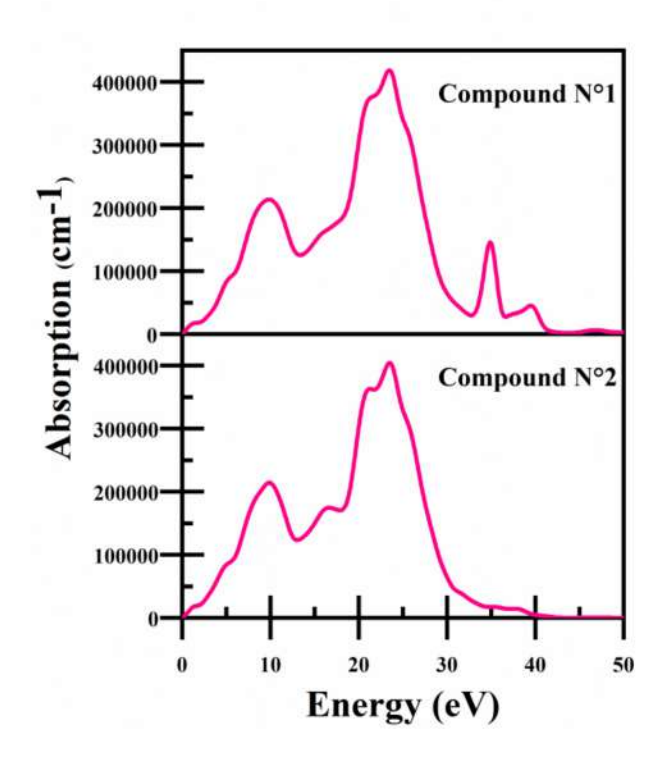


Figure III.17. Absorption coefficient behavior of Compound N°1 and Compound N°2.

The absorption coefficients, $\alpha(\omega)$ of Compound N°1 and Compound N°2 reveal strong photon–material interactions. Absorption begins from 0 eV and reaches peak values of 4.2×10^5 cm⁻¹ (Compound N°1) and 4.05×10^5 cm⁻¹ (Compound N°2) at 23.5 eV.

Both materials maintain $\alpha > 10^5$ cm⁻¹ from 6 eV to 29 eV, with major absorption peaks located around 10 eV and 23.5 eV. An additional peak appears at 35 eV for Compound N°1. These wide high-absorption regions indicate that both compounds can effectively absorb a broad range of high-energy photons. Furthermore, their transparency extends beyond 40 eV, affirming their potential for operation in extreme-UV regimes.

III.2.3.5. Energy Loss Function:

Figure III.18 illustrates the energy loss function spectra of Compound N°1 and N°2.

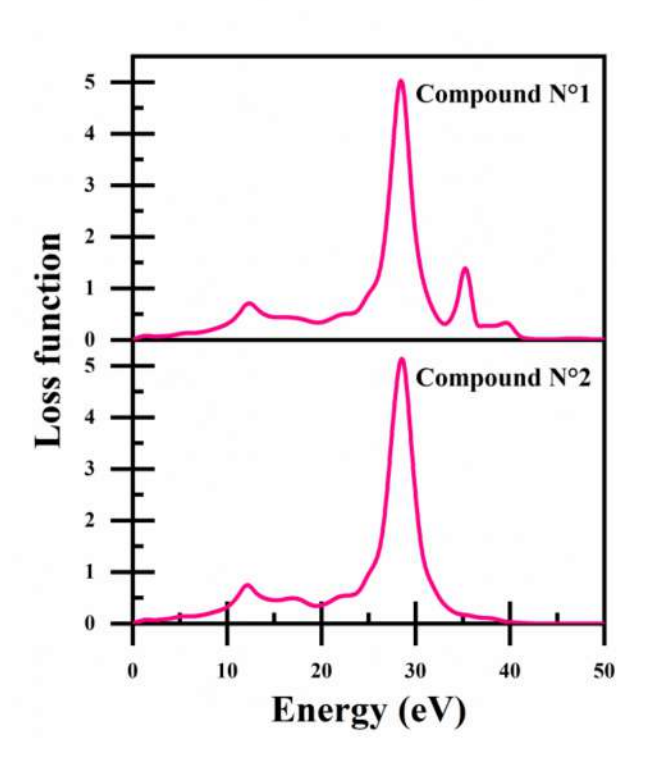


Figure III.18. Energy loss function for Compound N°1 and Compound N°2.

The energy loss spectra, which represent the energy lost by fast electrons traversing the material, exhibit dominant plasma resonance peaks at , with maximum intensities of 28.5 eV, with maximum intensities of 5.00 (Compound N°1) and 5.15 (Compound N°2). These peaks are associated with the collective oscillations of valence electrons (bulk plasmon).

Additional loss features are observed at 12.4, 35.15 and 39.5 eV, with Compound N°2 displaying a secondary peak at 12.15 eV. These indicate the presence of multiple excitation modes and interband transitions. Negligible energy loss is detected beyond 41.5 eV (Compound N°1) and 40 eV (Compound N°2), marking the upper bounds of electron energy dissipation.

III.2.3.6. Optical Conductivity:

The optical conductivity results of the studied compounds are presented in Figure III.19.

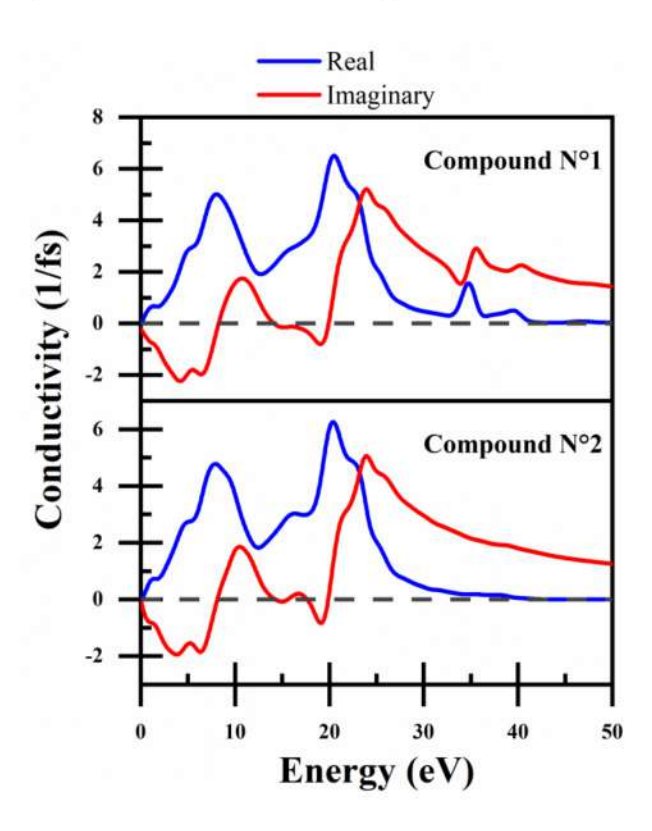


Figure III.19. Optical conductivity (real and imaginary part) profile of Compound N°1 and Compound N°2.

The optical conductivity spectra further highlight the strong interaction of these compounds with electromagnetic radiation. The real part, $\sigma_1(\omega)$, starts at 0 eV and reaches maxima of 6.8 (Compound N°1) and 6.25 (Compound N°2) at 20.5 eV and 20.4 eV, respectively. Notably, $\sigma_1(\omega)$ remains above 2 over the 4–25 eV range, confirming robust optical activity across this interval.

The imaginary part, $\sigma_2(\omega)$, also initiates from 0 eV and peaks at 5.25 (Compound N°1) and 5.10 (Compound N°2) near 24 eV. Additional features are identified at 10.75 eV, 35.5 eV (Compound N°1), and 10.5 eV (Compound N°2). Interestingly, both materials exhibit negative $\sigma_2(\omega)$ values in the ranges of 0–8.5 eV and 16–20 eV (Compound N°1), and 0–8.5 eV and 17.5–20 eV (Compound N°2), which may be indicative of plasmonic damping and anomalous dispersion effects.

III.2.3.7. Summary and Potential Applications:

The optical properties of Compound N°1 and Compound N°2 suggest that these materials have great potential for use in a variety of modern technologies. Their high ability to store electrical energy (as shown by their large dielectric constants) makes them suitable for use in electronic components such as capacitors and insulators[8]. Their strong interaction with light across a wide energy range, especially in the ultraviolet (UV) and extreme ultraviolet (EUV) regions, means they can be used in devices that need to detect or control highenergy light, such as UV detectors, solar-blind sensors, and protective eyewear or coatings that block harmful radiation[9]. Their high ability to bend and absorb light also makes them useful for improving the efficiency of solar cells and optical lenses[10]. Since they reflect a significant portion of light in the high-energy range, they could be applied as coatings on mirrors used in scientific instruments, space telescopes, or laser systems that operate at high energies[11]. The way they interact with light also suggests possible use in smart windows that control how much light and heat pass through, or in energy-efficient lighting systems. In addition, their optical responses suggest that they could help reduce radiation damage in sensitive electronics, especially in aerospace and medical environments. Overall, the wide range of light-related behaviors observed in these materials makes them promising for future applications in energy, electronics, sensing, and optical protection systems.

III.2.4. Mechanical properties:

Mechanical properties are crucial, as they reveal important aspects of a material's potential applications and define the limits and critical conditions for its use. Even materials with excellent electronic and optical properties may have limited practical applications if their mechanical behavior is not suitable under ambient conditions.

As explained in Chapter 2, the elastic constants matrix and the stiffness constants were calculated. Based on these, mechanical stability was evaluated, and various elasticity models were derived. The values of the elastic constants and stiffness constants are presented in the Table III.2.

Table III.2. The computed elastic constants of Compound N°1 and Compound N°2

| Compounds | Compo | und N°1 | Compound N°2 | | |
|-----------------------------------|-----------------|-----------------|-----------------|-----------------|--|
| Elastic / Stiffness | C _{ij} | S _{ij} | C _{ij} | S _{ij} | |
| constants | | | | | |
| C ₁₁ , S ₁₁ | 215.14650 | 0.0059013 | 156.71160 | 0.0090897 | |
| C ₂₂ , S ₂₂ | 257.43755 | 0.0052368 | 130.66040 | 0.0133753 | |
| C ₃₃ , S ₃₃ | 232.97830 | 0.0056466 | 186.01830 | 0.0094954 | |
| C ₄₄ , S ₄₄ | 71.83250 | 0.0139438 | 65.91355 | 0.0154664 | |
| C ₅₅ , S ₅₅ | 49.82380 | 0.0204019 | 46.12160 | 0.0219302 | |
| C ₆₆ , S ₆₆ | 80.88840 | 0.0123827 | 40.24530 | 0.0253307 | |
| C ₁₂ , S ₁₂ | 95.16777 | -0.0016119 | 69.11278 | -0.0028480 | |
| C ₁₃ , S ₁₃ | 83.31903 | -0.0013932 | 83.59795 | -0.0026006 | |
| C ₁₅ , S ₁₅ | -1.04422 | 0.0001620 | -7.82258 | 0.0013073 | |
| C ₂₃ , S ₂₃ | 104.53220 | -0.0018075 | 96.75895 | -0.0056763 | |
| C ₂₅ , S ₂₅ | -6.22893 | 0.0009321 | -3.41300 | 0.0004552 | |
| C ₃₅ , S ₃₅ | 8.57695 | -0.0012272 | -0.41880 | -0.0007749 | |
| C ₄₆ , S ₄₆ | -3.06245 | 0.0005279 | -7.11273 | 0.0027334 | |

III.2.4.1. Mechanical stability:

To verify the mechanical stability of our materials, we calculated the eigenvalues of the elastic constants matrix C by solving the characteristic equation:

$$\det(C - \lambda I) = 0$$

This equation yields six real eigenvalues, which are listed in the table III.3.

Table III.3. Calculated Eigenvalues (λ) of Compound N°1 and Compound N°2

| eigenvalues | λ_1 | λ_2 | λ_3 | λ_4 | λ_5 | λ_6 |
|--------------|-------------|-------------|-------------|-------------|-------------|-------------|
| Compound N°1 | 48.586 | 70.89410 | 81.82680 | 138.90987 | 141.64961 | 426.24058 |
| Compound N°2 | 38.406 | 45.02807 | 57.36207 | 67.75272 | 89.29548 | 327.82628 |

The table shows that all eigenvalues of the C matrix for both materials are positive, satisfying the general necessary and sufficient condition for mechanical stability.

III.2.4.2. Mechanical Moduli and related Physical Parameters:

The elastic moduli, such as the bulk modulus (B) and shear modulus (G), were calculated from the elastic constants using the formulas presented in Chapter II, based on the Voigt-Reuss-Hill approximation.

The values of Young's modulus (E), Poisson's ratio (ν), and the universal anisotropy index (A_u) were then determined using the bulk and shear moduli obtained from the Voigt, Reuss, and Hill averages. Additionally, the Debye temperature was calculated using its well-known relation, also described in Chapter II.

All these moduli and parameters are summarized in the table III.4.

Table III.4. Elastic and Mechanical Parameters of Compound N°1 and Compound N°2

| Mo | duli | Compound N°1 | Compound N°2 | Moduli | Compound N°1 | Compound N°2 |
|----|----------------|---------------------|--------------|--------------------------------|--------------|--------------|
| | B _v | 141.28893 | 108.03663 | Е | 174.41257 | 114.72116 |
| В | B _R | 139.67340 | 102.98126 | ν | 0.29308 | 0.31878 |
| | B _H | 140.48116 105.50894 | | B _H /G _H | 2.08303 | 2.42576 |
| | G_{v} | 68.67850 | 45.38413 | v_{t} | 3325.56039 | 2495.08137 |
| G | G_R | 66.20330 | 41.60616 | $v_{ m l}$ | 6146.76516 | 4837.56142 |
| | G _H | 67.44090 | 43.49514 | $v_{ m m}$ | 3711.33711 | 2793.67771 |
| A | 7 _n | 0.19851 | 0.50311 | θ_{D} | 468.19125 | 352.90664 |

We can recognize that Compound $N^{\circ}1$ exhibits a higher bulk modulus ($B_{H} = 140.5$ GPa) compared to Compound $N^{\circ}2$ ($B_{H} = 105.5$ GPa), indicating that Compound $N^{\circ}1$ has a denser and less compressible structure. This reflects stronger interatomic bonding within the lattice of Compound $N^{\circ}1$. These findings suggest that both materials, especially Compound $N^{\circ}1$, are promising candidates for applications requiring high mechanical strength or resistance to pressure-induced deformation.

Similarly, in terms of shear modulus, Compound $N^{\circ}1$ again demonstrates better performance ($G_H = 67.4 \text{ GPa}$) than Compound $N^{\circ}2$ ($G_H = 43.5 \text{ GPa}$). This implies that Compound $N^{\circ}1$ is more resistant to shear-induced distortion, offering greater mechanical rigidity. These results indicate that Compound $N^{\circ}1$ is particularly suitable for applications involving mechanical loading or structural demands, while Compound $N^{\circ}2$, with its relatively lower stiffness, may be better suited for roles where moderate flexibility is beneficial.

Among the studied compounds, Compound $N^{\circ}1$ displays a significantly higher stiffness (E = 174.4 GPa) compared to Compound $N^{\circ}2$ (E = 114.7 GPa), confirming the superior rigidity of the Compound $N^{\circ}1$. This makes Compound $N^{\circ}1$ particularly promising for mechanical applications where minimal deformation under load is essential.

The ductility of the studied compounds can be effectively assessed through both Poisson's ratio (ν) and Pugh's ratio (B_H/G_H), which offer complementary insights. The Figure III.20 shows the assessment of Ductility in Compound N°1 and N°2 via Poisson's and Pugh's Criteria. The Poisson's ratio values 0.293 for Compound N°1 and 0.319 for Compound N°2 exceed the conventional ductility threshold of 0.26, suggesting that both materials are capable of undergoing considerable plastic deformation before failure. Similarly, the B_H/G_H ratios for the same compounds 2.08 for Compound N°1 and 2.43 for Compound N°2 surpass the critical value of 1.75, further confirming their ductile nature. These indicators together imply that while both materials are ductile, Compound N°2 may exhibit slightly greater plastic deformability.

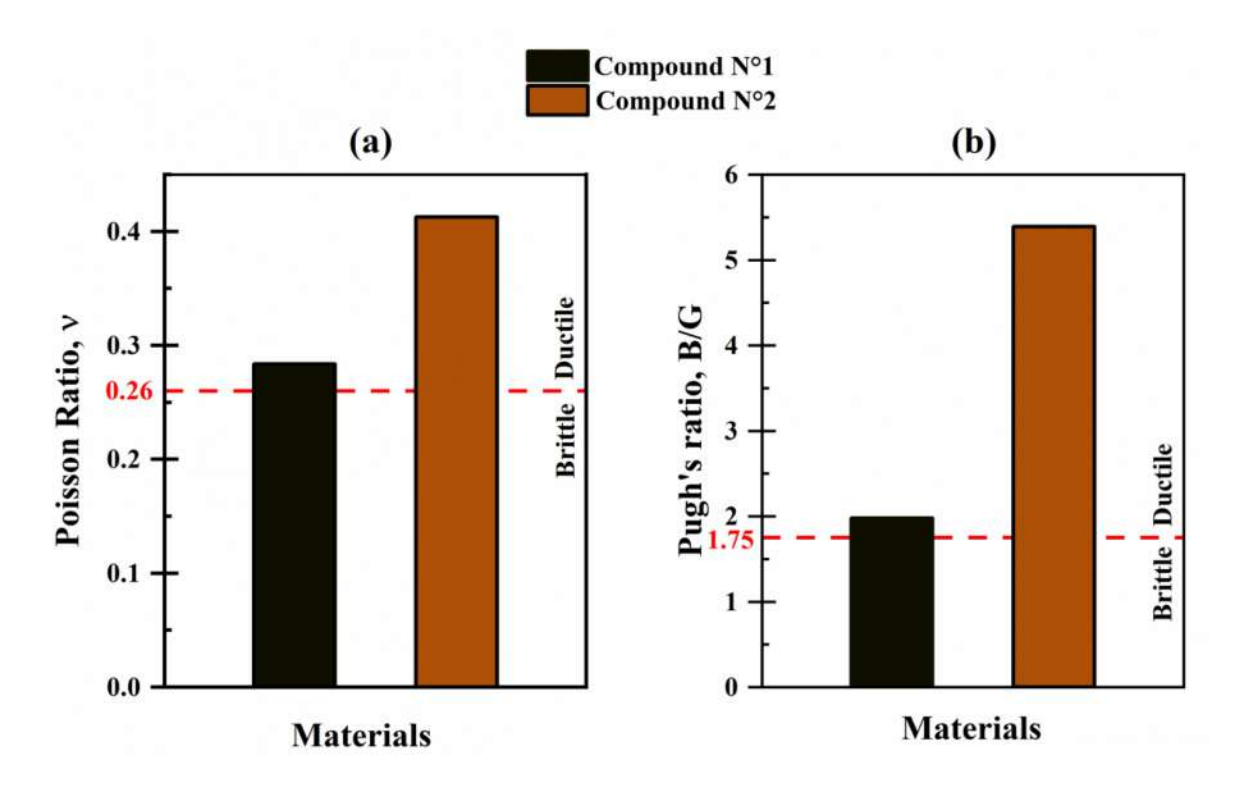


Figure III.20. Poisson's and Pugh's Ratios for Compound N°1 and Compound N°2.

Regarding elastic anisotropy, the Universal anisotropy index (A^U) reveals that Compound $N^{\circ}1$ ($A^U=0.20$) is more elastically isotropic than Compound $N^{\circ}2$ ($A^U=0.50$), which may lead to more uniform mechanical behavior in different crystallographic directions. This reinforces the mechanical stability and structural balance of Compound $N^{\circ}1$, making it particularly suitable for applications requiring both stiffness and isotropic mechanical response under complex loading conditions.

The acoustic properties of materials expressed through sound velocities and Debye temperature reflect their elastic stiffness and lattice dynamics. In this regard, Compound N°1 demonstrates superior behavior, with the highest transverse ($v_t = 3325.6 \, \text{m/s}$), longitudinal ($v_l = 6146.8 \, \text{m/s}$), and mean sound velocity ($v_m = 3711.3 \, \text{m/s}$), indicating stronger interatomic bonding and greater rigidity. Compound N°2 shows noticeably lower values in all three velocities, suggesting a comparatively softer lattice. This trend is also reflected in the Debye temperature (θ_D), a measure closely linked to lattice stiffness and thermal conductivity. Compound N°1 exhibits the highest θ_D of 468.2 K, followed by Compound N°2 at 352.9 K. These results suggest that Compound N°1 compound may be better suited for thermal management applications or high-frequency acoustic devices, where high phonon velocities and thermal stability are advantageous.

Between the two compounds, Compound N°1 consistently demonstrates superior mechanical performance compared to Compound N°2, as evidenced by its higher bulk, shear, and Young's moduli, greater sound velocities, and elevated Debye temperature. These characteristics indicate that Compound N°1 possesses stronger interatomic bonding, higher stiffness, and greater resistance to both compressive and shear stresses. Consequently, Compound N°1 is well-suited for applications requiring high mechanical strength, dimensional stability, and thermal resilience, such as structural components in harsh or high-pressure environments, thermal barrier coatings, or acoustic devices. In contrast, the relatively lower stiffness and higher ductility of Compound N°2 suggest its potential use in flexible or moderately deformable components, where mechanical adaptability is beneficial, such as shock-absorbing layers, buffer materials, or devices operating under moderate mechanical loads.

| Chapter III | : K | lesults | and | discussions |
|-------------|-----|---------|-----|-------------|
|-------------|-----|---------|-----|-------------|

III.2.5. Phonon:

Bibliographic references:

- [1] K. Momma, F. Izumi, VESTA 3 for three-dimensional visualization of crystal, volumetric and morphology data, Article, Applied Crystallography, 44 (2011).
- [2] K. Momma, F. Izumi, VESTA: a three-dimensional visualization system for electronic and structural analysis, Article, Applied Crystallography, 41 (2008).
- [3] S.J. Clark, M.D. Segall, C.J. Pickard, P.J. Hasnip, M.I. Probert, K. Refson, M.C. Payne, First principles methods using CASTEP, Article, Zeitschrift für kristallographie-crystalline materials, 220 (2005).
- [4] M. Segall, P.J. Lindan, M.a. Probert, C.J. Pickard, P.J. Hasnip, S. Clark, M. Payne, First-principles simulation: ideas, illustrations and the CASTEPcode, Article, Journal of Physics: Condensed Matter, 14 (2002).
- [5] R. Charif, R. Makhloufi, S.C. Mouna, A. Chadli, A. Barkat, M. Nouiri, Structural, electronic, optical, mechanical, and phononic bulk properties of tetragonal trirutile antimonate MSb2O6 (M= Fe, Co, Ni, or Zn): a first-principles prediction for optoelectronic applications, Article, Physica Scripta, 99 (2024).
- [6] M. Meunier, S. Robertson, Materials studio 20th anniversary, Article, Molecular Simulation, 47 (2021).
- [7] M. Fox, Optical properties of solids, Book, Oxford university press (2010).
- [8] F. Zheng, J. Tao, A.M. Rappe, Frequency-dependent dielectric function of semiconductors with application to physisorption, Article, Physical Review B, 95 (2017).
- [9] A.J. Corso, M.G. Pelizzo, Extreme ultraviolet multilayer nanostructures and their application to solar plasma observations: A review, Article, Journal of nanoscience and nanotechnology, 19 (2019).
- [10] Z. Shi, A.H. Jayatissa, Perovskites-based solar cells: A review of recent progress, materials and processing methods, Article, Materials, 11 (2018).
- [11] T. Sandner, J.U. Schmidt, H. Schenk, H. Lakner, M. Yang, A. Gatto, N. Kaiser, S. Braun, T. Foltyn, A. Leson, Highly reflective optical coatings for high-power applications of micro scanning mirrors in the UV-VIS-NIR spectral region, Conference, Society of Photo-Optical Instrumentation Engineers (SPIE) (2006).

GENERAL CONCLUSION

GENERAL CONCLUSION

This thesis presented a comprehensive experimental and theoretical study of two novel triple perovskite compounds, aimed at evaluating their potential for optoelectronic and energy-related applications.

Experimentally, both compounds were successfully synthesized using the solid-state reaction method and characterized by XRD, FTIR, and UV-Vis spectroscopy. Structural analysis confirmed the formation of single-phase perovskites. Optical measurements revealed that Compound N°1 exhibits a broader absorption range and a lower band gap than Compound N°2, making it more promising for light-harvesting and photocatalytic applications.

Theoretical investigations, based on DFT using the CASTEP code, provided insight into their structural, electronic, optical, mechanical, and vibrational properties. Geometry optimization led to a monoclinic configuration. Electronic structure calculations showed metallic behavior and spin asymmetry in both materials, suggesting potential magnetic characteristics. The absence of a clear band gap in the computed spectra is attributed to the use of the GGA-PBE functional, known for underestimating band gaps. Future work should consider more advanced methods such as hybrid functionals.

The optical properties, particularly of Compound N°1, demonstrated strong light-matter interaction, supporting its use in UV photodetectors, plasmonic devices, and optoelectronic systems. Mechanical analysis confirmed that both materials are ductile, anisotropic, and elastically stable, with Compound N°1 showing superior stiffness and thermal performance. Phonon calculations for Compound N°2 revealed imaginary modes, indicating dynamic instability in its relaxed structure.

The findings contribute to the growing interest in complex perovskite oxides and lay the groundwork for future development of materials tailored for optoelectronic, photovoltaic, magneto-optical, and protective coating technologies.

Abstract

This thesis presents a combined experimental and theoretical investigation of two triple perovskite compounds, Compound N°1 and Compound N°2, to assess their potential for optoelectronic and energy-related applications. The materials were synthesized by solid-state reaction and characterized using XRD, FTIR, and UV-Vis spectroscopy. Structural analysis confirmed the formation of perovskite phases, and optical measurements showed that Compound N°1 exhibits a broader absorption range and lower band gap than Compound N°2 counterpart, indicating stronger potential for light-harvesting applications.

Density Functional Theory (DFT) calculations provided insight into the structural, electronic, optical, and mechanical properties. Although the GGA-PBE functional underestimated the band gaps, both compounds exhibited strong optical activity. Compound N°1 demonstrated superior mechanical strength, ductility, and thermal stability compared to Compound N°2. Moreover, Phonon calculations for Compound N°2 revealed imaginary modes, suggesting that its monoclinic structure may be metastable and require specific synthesis conditions to be realized.

Résumé

Ce mémoire présente une étude expérimentale et théorique combinée de deux composés pérovskites triples, les composés N°1 et 2, dans le but d'évaluer leur potentiel pour des applications optoélectroniques et énergétiques. Les matériaux ont été synthétisés par réaction à l'état solide et caractérisés par XRD, FTIR et spectroscopie UV-Visible. L'analyse structurale a confirmé la formation des phases pérovskites, et les mesures optiques ont montré que le composé 1 possède une plage d'absorption plus large et une bande interdite plus faible que son homologue de composé 2, indiquant un meilleur potentiel pour les applications de conversion de lumière.

Les calculs basés sur la théorie de la fonctionnelle de la densité (DFT) ont permis d'explorer les propriétés structurales, électroniques, optiques et mécaniques. Bien que l'approximation GGA-PBE ait sous-estimé les bandes interdites, les deux composés ont montré une forte activité optique. Le composé 1 a démontré une meilleure résistance mécanique, une plus grande ductilité et une meilleure stabilité thermique que le composé 2. En outre, les calculs de phonons pour le composé 2 ont révélé des modes imaginaires,

suggérant que sa structure monoclinique pourrait être métastable et nécessiter des conditions spécifiques de synthèse pour être stabilisée.

الملخص

يتناول هذا البحث دراسة تجريبية ونظرية مشتركة لمركبين من البيروفسكايت الثلاثي، المركب 1 والمركب 2، بهدف تقييم إمكانياتهما في التطبيقات البصرية الإلكترونية ومجالات الطاقة. تم تحضير المركبين باستخدام طريقة التفاعل في الحالة الصلبة، وتمت دراستهما باستخدام تقنيات XRD، وFTIR، والتحليل الطيفي بالأشعة فوق البنفسجية – المرئية. أكدت التحاليل البنيوية تكوين طور البيروفسكايت، كما أظهرت القياسات البصرية أن المركب 1 يمتلك نطاق امتصاص أوسع وفجوة طاقة أقل مقارنة بالمركب 2 ، مما يشير إلى إمكانيات أفضل في امتصاص الضوء.

وقرت حسابات نظرية دالية الكثافة الوظيفية (DFT) فهماً لخصائص المركبات البنيوية والإلكترونية والبصرية والميكانيكية. وعلى الرغم من أن دالية GGA-PBE قللت من قيمة فجوة الطاقة، إلا أن كلا المركبين أظهرا نشاطاً بصرياً جيداً. كما أظهر المركب 1 تفوقاً في القوة الميكانيكية، والليونة، والاستقرار الحراري مقارنةً به المركب 2 وجود أنماط تخيلية، مما يشير إلى أن بنيته الأحادية الميل قد تكون شبه مستقرة، وتتطلب ظروف تحضير خاصة لتحقيق الاستقرار.